Scientific Research Publishing

International Journal of Geosciences, 2026, 17(11), 915-950
https://www.scirp.org/journal/ijg
ISSN Online: 2156-8367
ISSN Print: 2156-8359

EPMA-Constrained Multi-Stage Evolution and Uranium Metallogeny of Pegmatoid Leucosomes, Dudhi Granitoid Complex, Sonbhadra District, India

Ashokaditya P. Dhurandhar

Orion Geohytech, Nagpur, India
Email: apdhurandhar@gmail.com

How to cite this paper: Dhurandhar, A.P. (2026) EPMA-Constrained Multi-Stage Evolution and Uranium Metallogeny of Pegmatoid Leucosomes, Dudhi Granitoid Complex, Sonbhadra District, India. *International Journal of Geosciences*, **17**, 915-950.
https://doi.org/10.4236/ijg.2026.1711043

Received: September 15, 2026
Accepted: November 21, 2026
Published: November 24, 2026

Copyright © 2026 by author(s) and Scientific Research Publishing Inc.
This work is licensed under the Creative Commons Attribution International License (CC BY 4.0).
http://creativecommons.org/licenses/by/4.0/

Open Access

Abstract

Wavelength-dispersive electron-probe microanalysis (EPMA) and powder X-ray diffractometry (XRD) of rock-forming silicates (biotite, alkali feldspar, plagioclase) and accessory minerals (uraninite, zircon, titanates) from uraniferous pegmatoid leucosome mobilisates (PLM) across the Dudhi Granitoid Complex (Jura, Jaurahi, Kudri, Anjangira-Deohar, Dolatola, and Lakhar), northwestern Chhotanagpur Granite Gneiss Complex (CGGC), resolve a protracted polymetamorphic ($M1$ - $M4$) and polydeformational ($D1$ - $D5$) history. Biotites across all suites classify as annite-rich (X_{Ann} = 0.54 - 0.84; Fe/(Fe + Mg) = 0.60 - 0.82). Titanium-in-biotite thermometry yields 668˚C - 695˚C at 4.3 - 5.7 kbar for the main PLM suite (Jaurahi, Jura, Anjangira), 698˚C - 702˚C at 2.07 - 2.55 kbar for the Kudri Hills leucosome/melanosome, and 680˚C at 2.49 kbar for the Lakhar PLM under reducing conditions ($\log fO_2$ = −16.0 to −19.8 bars); a single Dolatola sample records retrograde re-equilibration at 535˚C - 540˚C (6.4 kbar). Feldspar mineral chemistry demonstrates primary potassic alkali feldspar (Or86 - 97) and oligoclase-andesine (An20 - 44), overprinted by metasomatic hydrothermal albite (Ab90 - 98, An < 5) and albitisation that lowered orthoclase content to Or53. Zircon exhibits pronounced magmatic fractionation: Zr/Hf collapses from near-chondritic values (33 - 36) down to 18.9 - 23.9 at Dolatola and late Jaurahi, with HfO_2 reaching 2.75 wt% and UO_2 reaching 1.98 wt%. CHIME chemical dating of Lakhar zircon resolves inherited Mesoarchaean to Palaeoproterozoic xenocryst cores (2892 Ma, 2269 Ma), syn-collisional anatectic crystallization (1846 - 1835 Ma), and Mesoproterozoic thermal resetting (1402 Ma, 1214 Ma), alongside metamict Phanerozoic lead-loss domains (116 - 159 Ma). Uraninites define two genetic populations: primary magmatic Type-I uraninite (UO_2 = 73.4 - 85.6 wt%, ThO_2 = 2.3 - 7.8

wt%, CaO < 1.0 wt%, SiO_2 < 0.5 wt%) yielding chemical ages of 834 - 901 Ma across the Kudri sector and Lakhar (841 ± 62 Ma), and metasomatic Type-II high-Ca uraninite at Anjangira (CaO = 3.66 - 10.69 wt%, mean 7.39 wt%; UO_2 = 71.4 - 78.4 wt%) yielding shifted chemical ages of 621 - 812 Ma (mean 731 Ma). Precision unit-cell parameters (a_0 = 5.4485 - 5.4694 Å) verify that all primary uraninites occupy the metamorphic fluorite field (MTM), recording lattice contraction driven by post-crystallisation auto-oxidation ($UO_{2.01} \rightarrow UO_{2.19}$). An integrated five-stage geodynamic model places primary volatile-fluxed melt concentration at ~1850 - 1630 Ma during collision within the Central Indian Tectonic Zone (CITZ), isobaric cooling at ~1648 Ma, Grenvillian tectonometamorphic re-equilibration and uraninite crystallization at 1200 - 950 Ma, and brittle reactivation along the Son-Narmada South Fault (SNSF) driving sodic-calcic metasomatism at 950 - 600 Ma.

Keywords

Uraninite Chemical Dating, Biotite Thermobarometry, Dudhi Granitoid Complex, Zircon Petrochronology, Sodic Metasomatism, Son-Narmada South Fault, Central Indian Tectonic Zone

1. Introduction

The northwestern fringe of the Chhotanagpur Granite Gneiss Complex (CGGC) in Sonbhadra District, Uttar Pradesh, exposes radioactive pegmatoid leucosome mobilisates (PLM) hosted within migmatitic, granitic, and metasedimentary rocks of the Palaeoproterozoic Dudhi Group [1] [2]. These mobilisates are localized along an ENE-WSW tectonic corridor controlled by the lithospheric-scale Son-Narmada South Fault (SNSF), which defines the southern structural boundary of the Mahakoshal rift belt within the Central Indian Tectonic Zone (CITZ) [3] [4]. The CITZ represents an expansive orogenic suture belt recording the accretion of the Northern Indian Block (Bundelkhand Craton) to the Southern Indian Block (Bastar and Dharwar cratons) during the assembly and dispersal of the Columbia and Rodinia supercontinents between ~2.1 and 0.9 Ga [5]-[7].

The uranium systems of the Dudhi Granitoid Complex belong to the class of structurally controlled, granite- and migmatite-related rare-element pegmatite deposits [8]-[11]. Earlier reconnaissance and mineralogical studies identified radioactive anomalies and preliminary ages across individual prospects including Jura, Kudri, Naktu, and Anjangira [1] [12]-[15]. Recent advances in petrochronology have demonstrated that the Dudhi granitoids preserve protolith accretion events between 1708 and 1756 Ma and that accessory zircons underwent extreme geochemical fractionation [15].

Nevertheless, systematic resolution of the polymetamorphic ($M1$ - $M4$) and polydeformational ($D1$ - $D5$) history requires an integrated approach. Three primary questions are evaluated in this paper:

1) What were the exact pressure-temperature (*P-T*) regimes during leucosome crystallization and subsequent retrograde overprinting across the various structural sectors?

2) How do the mineral chemistry and crystallographic parameters of primary and metasomatic uraninite differentiate between peak magmatic-anatectic crystallization and hydrothermal fluid infiltration?

3) How are the compiled geochronological age peaks partitioned between Palaeoproterozoic crustal anatexis, Grenvillian tectonothermal reworking, and Neoproterozoic-Phanerozoic brittle fault reactivation along the SNSF?

2. Geological, Structural, and Deformational Framework

2.1. Regional Lithotectonic Framework

The Dudhi Granitoid Complex occupies the northern margin of the CGGC, lying immediately south of the SNSF. Four principal lithotectonic units are exposed in the study area (Figure 1):

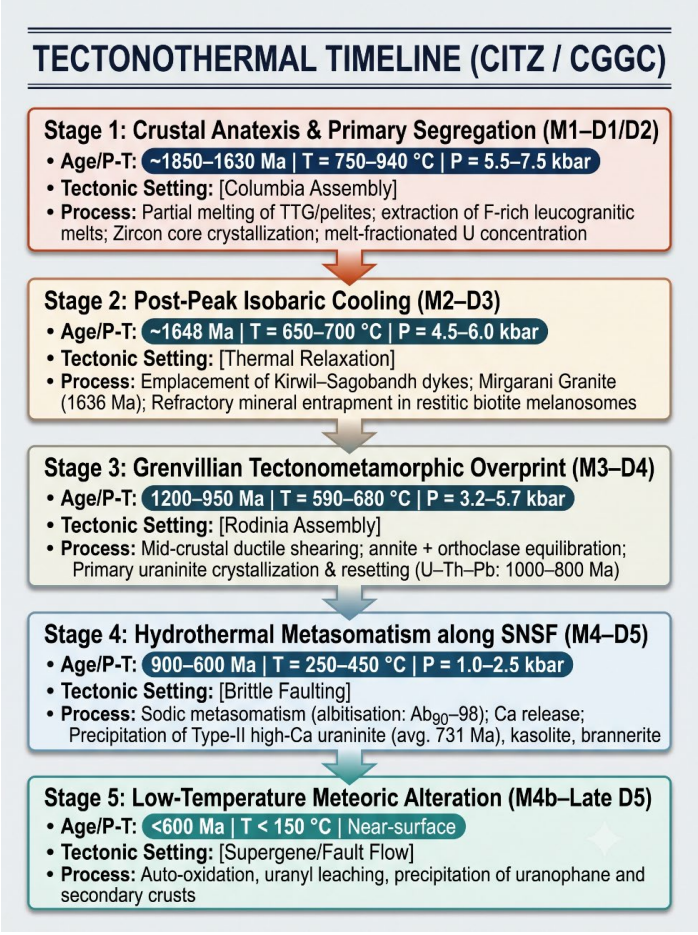


Figure 1. Tectonothermal timeline CITZ/CGGC.

- **Archaean to Palaeoproterozoic Basement Complex:** Composed of tonalite-trondhjemite-granodiorite (TTG) gneisses, migmatitic paragneisses, and silli-

manite-orthoclase metapelites. Inherited zircon xenocryst cores within this basement preserve residual protolith ages ranging from 3485 to 2500 Ma [16].

- **Syn- to Post-Tectonic Granitoids:** Prominently represented by the Dubha Granite (1754 ± 116 Ma) [17], and the Mirgarani Granite (1636 ± 66 Ma) [12], recording syn-collisional anatexis and subsequent post-orogenic plutonism.
- **Metabasic Dykes and Sills:** Post-peak tholeiitic dyke swarms, including the Kirwil-Sagobandh suite (1648 ± 112 Ma) [18], marking terrane-scale isobaric cooling (IBC) and thermal relaxation.
- **Pegmatoid Leucosome Mobilisates (PLM):** Radioactive quartzofeldspathic mobilisates, albite-rich pegmatoids, and biotite melanosome selvedges injected along structural dilation zones across the Jura, Anjangira-Deohar, Jaurahi, Kudri, Dolatola, and Lakhar sectors [1] [2] [19].

2.2. Polydeformational Sequence (*D*1 - *D*5) and Metamorphic Stages (*M*1 - *M*4)

Structural mapping identifies five ductile to brittle deformational events (*D*1 - *D*5) linked with four metamorphic episodes (*M*1 - *M*4), summarized in Table 1 and Table 2.

Table 1. Polydeformational events (*D*1 - *D*5), fabric elements, metamorphic correlates, and tectonic significance in the dudhi granitoid complex.

Deformation Phase	Structural Style & Fabric Elements	Regional Orientation	Metamorphic Correlation	Age Constraint	Tectonic Significance
*D*1	Layer-parallel ductile shearing; penetrative *S*1 gneissic foliation; isoclinal folding (*F*1)	ENE-WSW striking; subvertical dips	*M*1 (Granulite to upper-amphibolite)	~1850 - 1630 Ma	Collisional assembly of CITZ (Columbia); high-*T* crustal anatexis
*D*2	Coaxial compression; asymmetric tight *F*2 folds; pervasive *S*2 axial-planar cleavage	ENE-WSW axial surfaces; sub-vertical dips	*M*1 (Late anatectic segregation)	~1850 - 1630 Ma	Syn-kinematic injection of pegmatoid leucosomes along fold hinges and shears
*D*3	Upright, open to gentle refolding (*F*3); terrane-scale cross-warping	NW-SE to N-S axial traces	*M*2 (Retrograde isobaric cooling)	1648 ± 112 Ma	Post-orogenic thermal relaxation; emplacement of Kirwil-Sagobandh dykes
*D*4	Ductile-to-brittle shearing; mylonitic bands along ancestral SNSF	ENE-WSW corridor; localized microfracturing	*M*3 (Amphibolite facies overprint)	1200 - 950 Ma	Grenvillian crustal reworking; thermal and dynamic re-equilibration of silicates
*D*5	Pervasive brittle faulting; brecciation; cataclasis and fault gouge	High-permeability channelways along SNSF	*M*4 (Hydrothermal metasomatism)	950 - 600 Ma & <600 Ma	Brittle reactivation; Na-Ca metasomatism, feldspar albitisation, uraninite alteration

Table 2. Polymetamorphic phases (*M*1 - *M*4), pressure-temperature regimes, and mineralogical correlates.

Metamorphic Phase	Temperature (*T*, °C)	Pressure (*P*, kbar)	Age Constraint	Structural Stage	Mineral Assemblage and Petrogenetic Process
***M*1 Peak Anatexis**	750 - 940	5.5 - 7.5	~1850 - 1630 Ma	Syn-*D*1/*D*2	Dehydration melting of metapelitic/TTG crust; monazite/apatite saturation; primary U^{4+} uraninite and zircon core growth
***M*2 Isobaric Cooling**	650 - 700	4.5 - 6.0	1648 ± 112 Ma	Syn-*D*3	Clockwise isobaric cooling path; Kirwil-Sagobandh dykes; elemental uptake in restitic biotite melanosome selvedges
***M*3 Grenvillian Overprint**	590 - 680	3.2 - 5.7	1200 - 950 Ma	Syn-*D*4	Amphibolite-facies transpressional shearing; equilibration of annite-rich biotite, orthoclase, and low-Zr/Hf zircon rims
***M*4 Metasomatic/ Hydrothermal**	450 down to <150	1.0 - 2.5	950 - 600 Ma & <600 Ma	Syn-*D*5	Brittle faulting along SNSF; hydrothermal albitisation (Ab90 - 98), Ca-release, precipitation of Type-II uraninite and kasolite

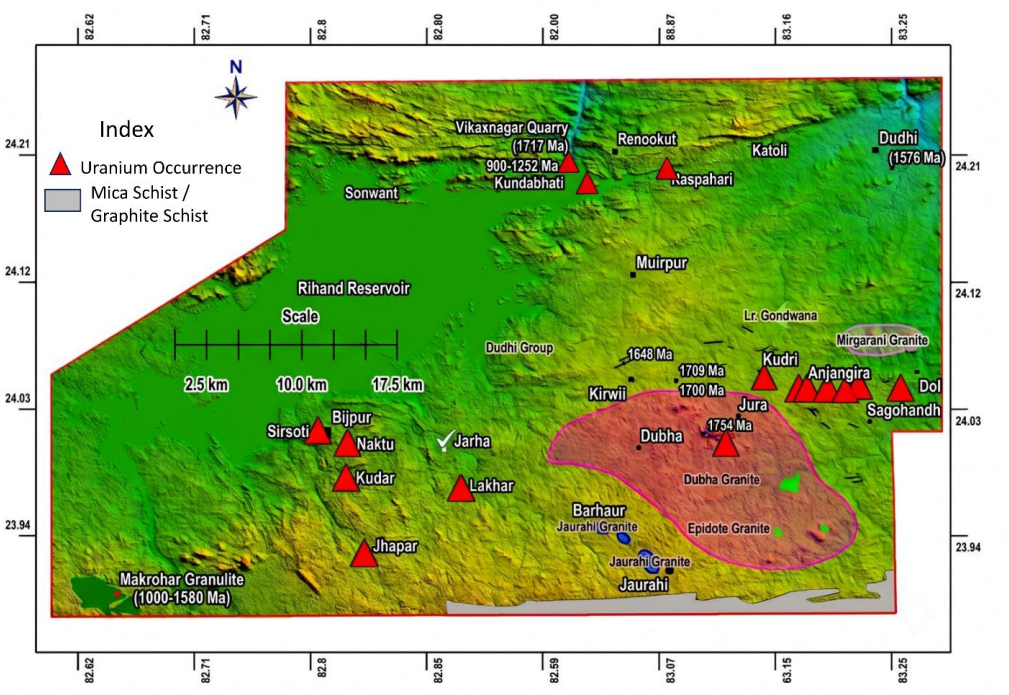


Figure 2. Regional geological map of the area.

Geological Setup

The Dudhi Granitoid Complex lies along the northwestern margin of the CGGC, juxtaposed against the Mahakoshal Group across the Son-Narmada South Fault (SNSF). Host rocks comprise porphyritic granite gneisses, migmatites and mica schists (Figure 2). Uraniferous PLM form concordant to discordant sheets, dykes and injection complexes that post-date the principal penetrative fabric but are af-

fected by late ductile-to-brittle shearing (Figures 3-6). Mineralogy is dominated by quartz, microcline-perthite, plagioclase and annitic biotite. Accessory phases include zircon, monazite and uraninite, with secondary kasolite. Pitchblende is used only for colloform uranium oxide where that texture was observed. Primary uranium is concentrated in the most fractionated, volatile-rich fractions. Phases not confirmed in this dataset are not listed here as identified minerals.

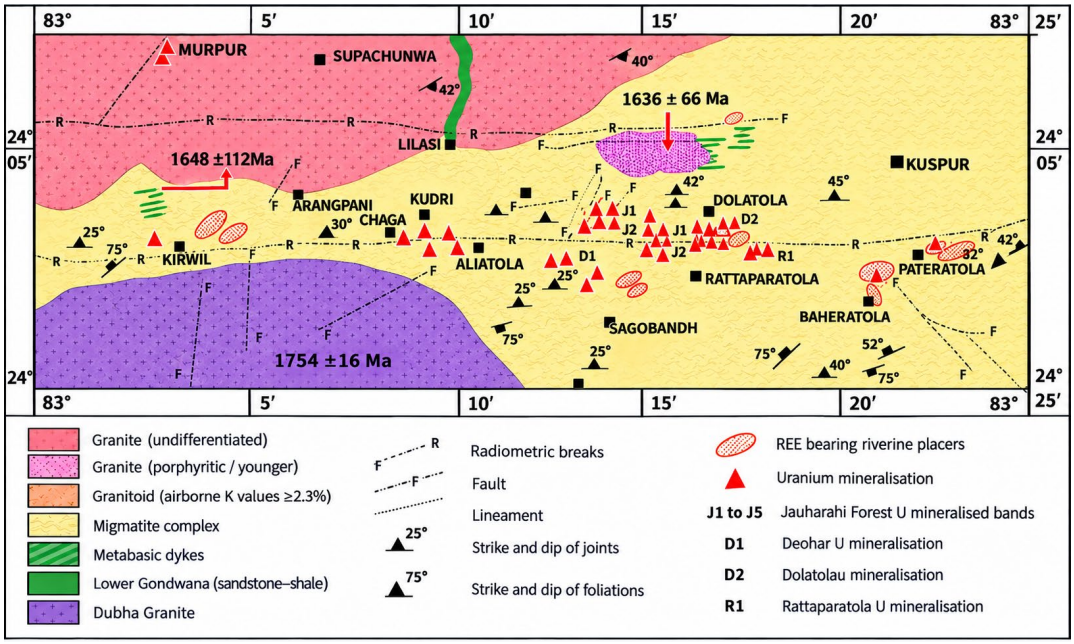


Figure 3. Geological map of the study area.

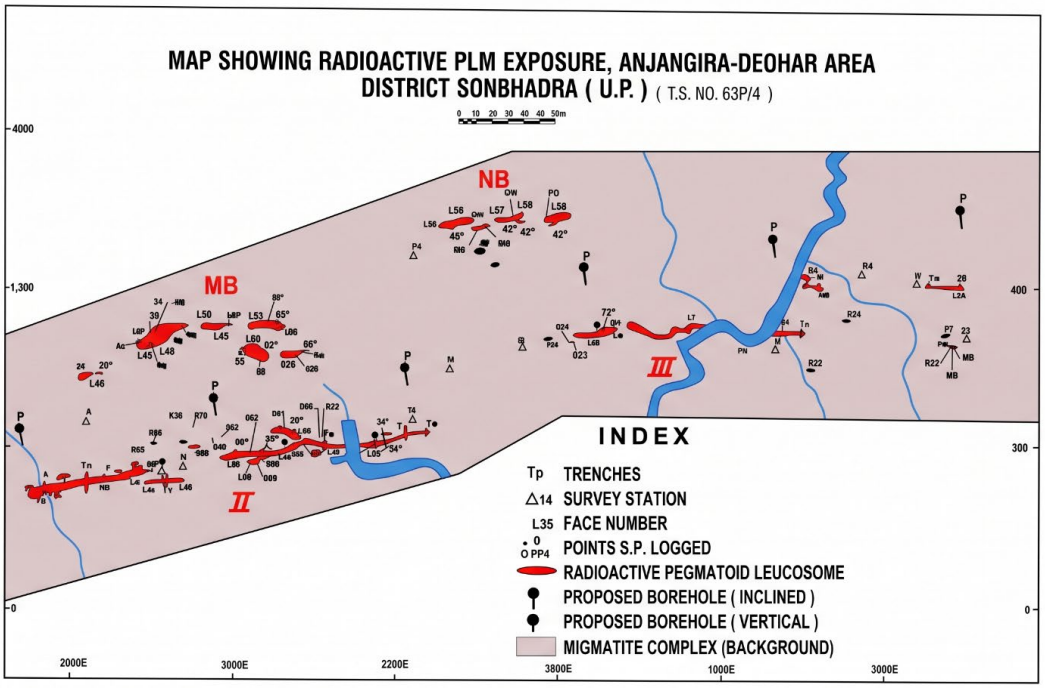


Figure 4. Geological map of the Anjangira-Deohar anomaly showing uraniferous pegmatoid leucosomes.

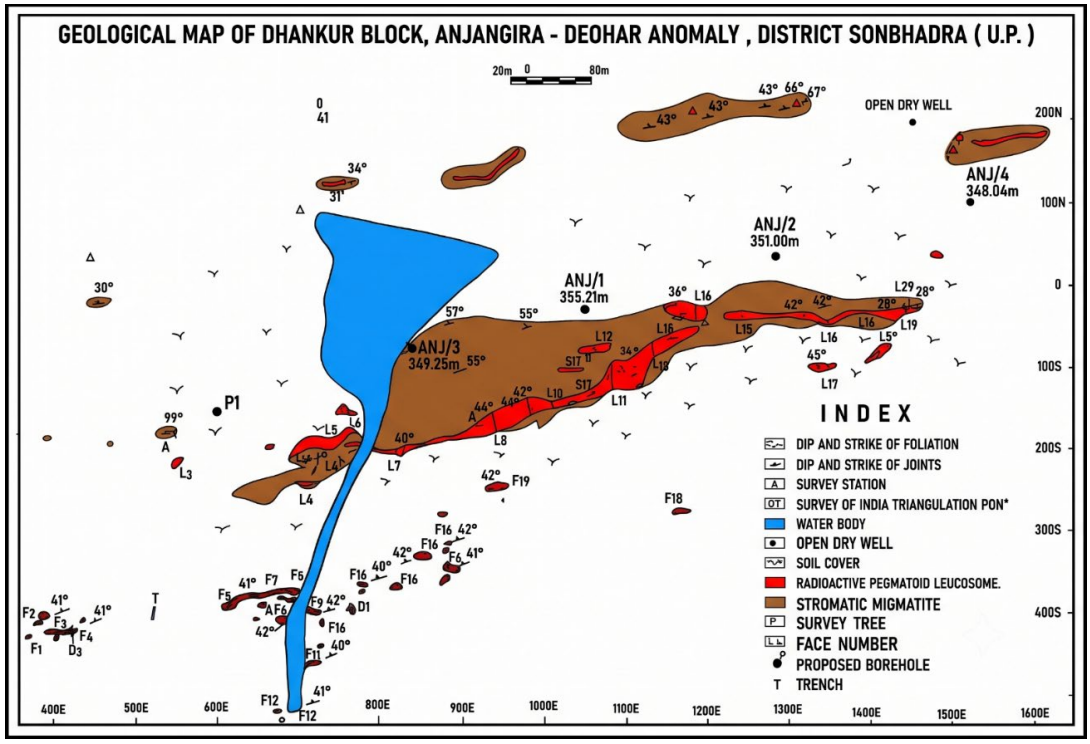


Figure 5. Geological map of area around Dhankur anomaly.

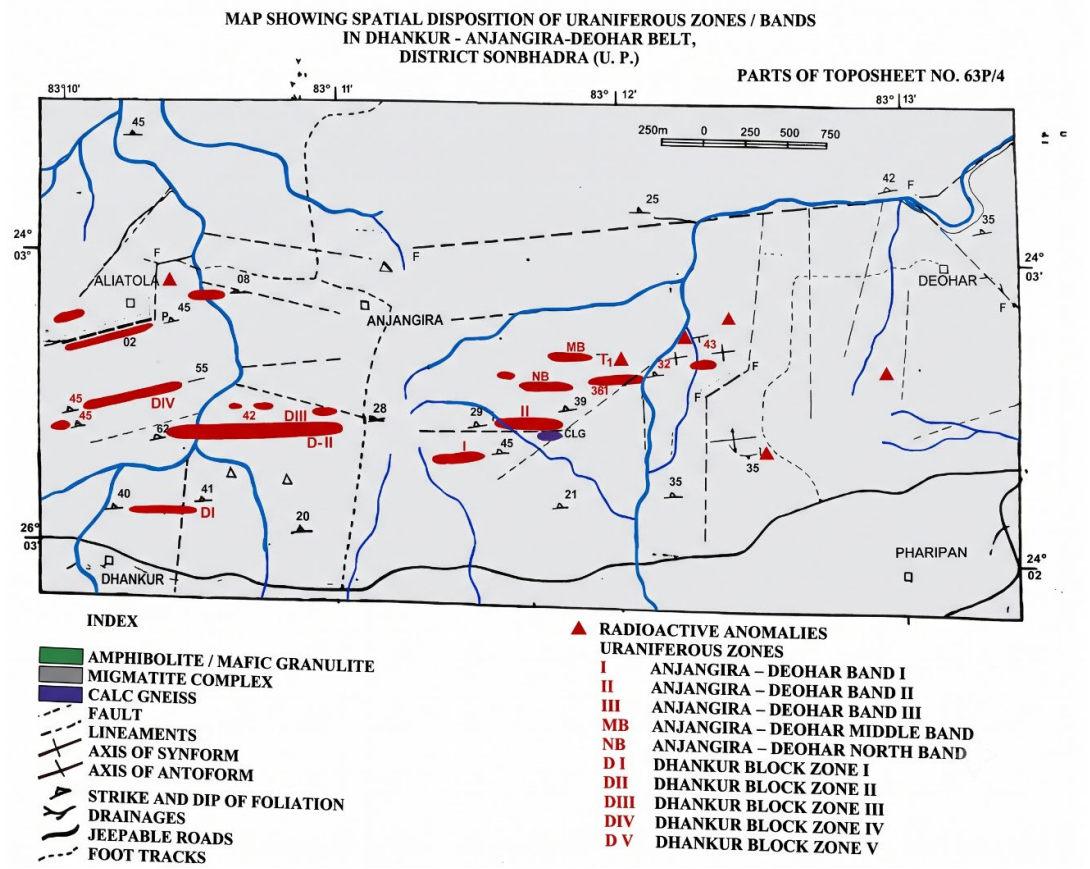


Figure 6. Spatial distribution of uriniferous zones/bands in Dhankhur-Anjangira - Deohar Belt.

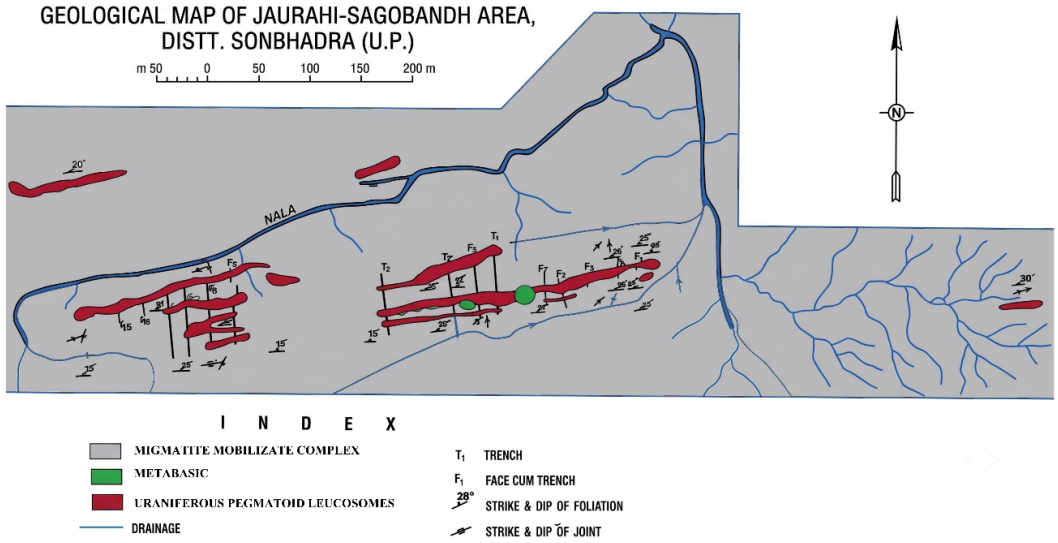


Figure 7. Geological map of area around Jaurahi Anomaly.

3. Materials and Methods

3.1. Sampling and Analytical Inventory

Field investigations and sampling were conducted across drill cores and surface exposures within Sonbhadra District, Uttar Pradesh:

- **Jaurahi Reserved Forest:** Northern Sagobandh sector, represented by porphyritic leucosome sample A-261 (JCH-1) and sheared pegmatoid mobilisate sample A-262 (JCW7-1) (Figure 7).
- **Jura Occurrence:** Uraniferous biotite-quartz-feldspar gneiss sample A-493 (JUR-1) and biotite rock/melanosome contact sample A-541, JUR-16 [15] (Figure 2).
- **Anjangira-Deohar Sector:** Radioactive PLM drill cores A-534, (AD-24), A-535 (AD-37), and A-536 (AD-40) [20] [21] (Figures 3-5).
- **Dolatola Prospect:** Highly evolved radioactive mobilisate sample A-537 (DTLA-4-1) (Figure 3).
- **Lakhar Sector:** Uraninite concentrate sample A-39 and coexisting pegmatoid leucosome gneiss sample A-39N (Figure 2) [21].
- **Kudri Hills:** Radioactive pegmatoid leucosome (Points 1 - 6) and restitic melanosome (Points 7 - 12) suites (Chhabra & Kumar, 2002 [12]) (Figure 2 and Figure 3).
- **Sirsoti:** Uraninite SIR-1 to SIR-9 uraniferous pegmatoid leucosome (Figure 2).

The analytical database generated comprises 24 spot analyses of biotite at Kudri and 12 at Lakhar; 8 representative sample averages for regional biotite; 43 feldspar analyses across 4 sample suites; 44 accessory zircon analyses; 12 single-spot zircon CHIME dating points on Lakhar rock A-39N; and 138 uraninite point analyses across 9 regional sectors. Additionally, 17 regional uraninite crystallographic refinements [22] are compiled.

3.2. Operating Conditions

Analyses of minerals were conducted using a CAMECA SX-50 EPMA with WDS, employing TAP, LIF, and PET crystals. The system had a 15 kV accelerating voltage, 40 nA beam current, 2 - 5 μm beam diameter, and 10 - 60 s counting time. Natural and manufactured mineral standards were employed for elemental peak calibrations. The PAP program rectified raw data. To reduce element interferences, all peak overlap adjustments were evaluated. Kα-lines for Na, Mg, Al, Si, P, K, Ca, Ti, Cr, Mn, Fe, Co, Ni, Cu, Zn; Lα lines for Mo, Ag, Cd, Sb, Ba, Y, La, Ce, Yb, Lu; Lβ-1ines for Pr, Nd, Sm, Gd, Tb, Dy, Ho, Er; Mα: lines for Th, Pb; and Mβ line for U Repeated analysis of standards revealed a relative error of less than 2 wt.% for major and minor element concentrations at 95% confidence. The calibration was routinely tested using MAC, UK's andradite standard [23] provide more details.

The analytical data of uraninite was compared to international mineral standards including UO_2, ThO_2, $MnTiO_3$, REE-fluorides, Y and silicates, etc. [24] recommended 10 s for U, 20 s for Th, and 40 s for Pb for analytical lines and half of this period for background counts on both sides of the peak. EPMA-based chemical ages were calculated assuming that U, Th, and total Pb remained in a closed system and that all Pb is radiogenic. We calibrated each element with at least three acquisitions. For chemical age computation, the error (2σ-level) is <1%, notably for Pb content over 20%. Using the empirical formula following [25], chemical ages were determined for each point (average of three) using U, Th, and Pb values. Calculated chemical age inaccuracies are mostly due to Pb count uncertainty [26].

Electron-probe microanalyses (EPMA) of uraninite, biotite, zircon, alkali feldspar and plagioclase were performed on polished thin sections. Structural formulae were calculated on standard oxygen bases (uraninite 2 oxygens; biotite 24 (O, OH); zircon 4 oxygens; feldspars 32 oxygens). Trace-element enrichments in Kudri biotite are taken from [12]. Chemical ages were calculated by the CHIME/Bowles methods; published U-Pb and Rb-Sr constraints are integrated where available.

- Biotites: Calculated on an anhydrous basis of 22 positive oxygen equivalents/24 anions (O, OH, F, Cl), fixing tetrahedral ΣZ = Si + Al_{IV} = 8.00 apfu [27] [28]. Total iron was measured as FeO (or converted using FeO = 0.8998 × Fe_2O_3).
- Feldspars: Normalized to 32 oxygens.
- Zircons: Normalized to 4 oxygens.
- Uraninites: Normalized on a fluorite-type single-cation solid solution basis and 2-oxygen (or 4-oxygen equivalent) stoichiometry [29].

3.3. Diagnostic Mineral Status

Mineral species designations adhere strictly to compositional stoichiometry and diagnostic petrographic textures (**Table 3**).

Table 3. Mineral identification status and criteria applied in this study.

Phase	Ideal Chemical Formula	Symmetry	Diagnostic Analytical Criterion	Status in this Study
Uraninite	UO_2 (to UO_{2+x})	Cubic, $Fm\bar{3}m$	UO_2 > 70 wt%, high Th/Y/REE; isometric crystal habit	**Confirmed.** Primary Type-I and metasomatic Type-II populations
Pitchblende	UO_2 (colloform)	Cubic	Botryoidal, colloform, low-Th habit	**Textural term only.** (Not an independent species)
Kasolite	$Pb(UO_2)SiO_4{\cdot}H_2O$	Monoclinic, $P21/c$	Stoichiometric Pb, U, and Si; alteration fringes around uraninite	**Confirmed.** Only verified secondary uranyl silicate
Brannerite	UTi_2O_6	Monoclinic, $C2/m$	U:Ti ≈ 1:2 atomic proportion; requires Ti-rich metasomatic fluid	**Inferred.** Present in Rihand Valley; unconfirmed in studied PLM
Uranophane	$Ca(UO_2)_2(SiO_3OH)_{2\cdot5}H_2O$	Monoclinic, $P21$	Ca-uranyl silicate; diagnostic 7.88 Å XRD reflection	**Inferred.** Supergene phase in regional literature
Coffinite	$U(SiO_4)_{1-x}(OH)_{4x}$	Tetragonal, $I41/amd$	Si:U ≈ 1:1; depleted Pb and Ca	**Inferred.** Secondary boundary phase
"Gummite"	Hydrated uranyl mixture	Amorphous / mixed	Non-stoichiometric fine-grained mixture of oxides/silicates	**Excluded.** Informal field term; not a mineral species

3.4. Thermobarometric Calibrations

Crystallization temperatures were determined via:

1) The semi-empirical titanium-in-biotite geothermometer of [30], calibrated for graphitic metapelitic rocks at 3 - 6 kbar:

$$T(^{\circ}\mathrm{C}) = \left[b\ln\left(\mathrm{Ti}_{11\mathrm{O}}\right) - a - c\left(X_{\mathrm{Mg}}\right)^3 \right]^{0.3333} \tag{1}$$

where $a = -2.3594$, $b = 4.6482 \times 10^{-9}$, $c = -1.7283$, $\mathrm{Ti}_{11\mathrm{O}} = \mathrm{Ti}_{22\mathrm{O}}/2$, and $X_{\mathrm{Mg}} = \mathrm{Mg}/(\mathrm{Mg} + \mathrm{Fe}^{2+})$.

2) The empirical titanium-in-biotite geothermometer of [31]:

$$T(\mathrm{K}) = 1.0337 - \left(\mathrm{Ti}/\mathrm{Fe}^{2+}\right)^{838} \tag{2}$$

Crystallization pressures were estimated using the total aluminium-in-biotite geobarometer of [32], calibrated for granitic rocks:

$$P(\mathrm{kbar}) = 3.03 \times \mathrm{Al}_{\mathrm{total(22O)}} - 6.53\left(\pm 0.33\ \mathrm{kbar}\right) \tag{3}$$

Depths were estimated assuming an average continental crustal density gradient of 3.7 km/kbar.

3.5. Chemical Dating Formulations and Precision Limits

U-Th-total Pb chemical ages were computed from the radioactive decay of ^{238}U, ^{235}U, and ^{232}Th into lead [26] [33]-[35]:

$$\begin{aligned} \mathrm{Pb} = \mathrm{U}\left[\frac{0.9928}{238.03}\times 206\left(\mathrm{e}^{\lambda_{238}t}-1\right)+\frac{0.0072}{235.04}\times 207\left(\mathrm{e}^{\lambda_{235}t}-1\right)\right] \\ +\mathrm{Th}\left[\frac{208}{232.04}\left(\mathrm{e}^{\lambda_{232}t}-1\right)\right] \end{aligned} \tag{4}$$

Adopted decay constants (Steiger & Jäger, 1977 [36]):

$$\lambda_{238} = 1.55125 \times 10^{-10}\ \text{yr}^{-1}, \lambda_{235} = 9.8485 \times 10^{-10}\ \text{yr}^{-1}, \lambda_{232} = 4.9475 \times 10^{-11}\ \text{yr}^{-1} \quad (5)$$

Stoichiometric conversion factors:

$$\text{U} = \text{UO}_2 \times 0.8815, \text{Th} = \text{ThO}_2 \times 0.8788, \text{Pb} = \text{PbO} \times 0.9283 \quad (6)$$

The empirical approximation of [33] was applied concurrently:

$$t\left(\text{Ma}\right) = \left(0.0884 \cdot \text{U}\right) + \left(0.0245 \cdot \text{Th}\right)\text{Pb} \times 10^3 \quad (7)$$

Analytical precision for EPMA chemical dating is constrained to ±5% - 15%; precision degrades in low-lead and metamict zones. No analysis is assigned a precision better than 1%.

4. Results I: Mineral Chemistry and Thermobarometry

4.1. Biotite Mineral Chemistry and *P-T* Conditions

Biotite compositions across the Dudhi Granitoid Complex are strongly enriched in iron (Table 4 and Table 5). Total FeO* ranges from 22.86 wt% at Jura (JUR-16) to 28.62 wt% at Dolatola (DTLA-4-1) and 28.29 wt% at Lakhar. The Fe/(Fe + Mg) ratio spans 0.60 to 0.82, and octahedral site annite proportions (X_{Ann} = $Fe^{2+}/(Fe^{2+} + Mg)$) range from 60.1 mol% to 82.3 mol% (or 54.1 - 68.6 mol% when normalized against total octahedral cations ΣY). This trend reflects progressive fractional crystallization of peraluminous, volatile-rich S-type granitic melts (Figure 8).

Table 4. Electron microprobe analyses (wt%) and recalculated structural formulae of biotites (22 Oxygen Basis).

Oxide/ Parameter	JCW7-1 (A-262)	JCH-1 (A-261)	JUR-1 (A-493)	AD-24 (A-534)	AD-37 (A-535)	AD-40 (A-536)	Dolatola (A-537)	JUR-16 (A-541)	Kudri Leu. (Av.)	Kudri Mel. (Av.)	Lakhar (Mean)
SiO_2	35.43	35.22	33.72	33.30	32.64	33.91	34.40	34.63	34.37	34.31	33.42
TiO_2	3.23	3.16	3.15	2.89	2.86	2.78	1.27	3.17	3.31	3.28	2.97
Al_2O_3	15.96	15.60	14.68	16.45	16.72	16.65	18.13	14.03	15.99	15.06	15.31
FeO*	25.40	24.41	25.13	26.25	26.35	26.90	28.62	22.86	27.88	27.89	28.29
MnO	0.24	0.13	0.16	0.13	0.13	0.21	0.63	0.34	0.29	0.28	0.48
MgO	5.80	6.92	6.04	4.60	5.41	5.65	4.15	8.40	4.49	5.30	3.44
CaO	0.04	0.06	0.01	0.06	0.06	0.13	0.58	0.04	0.01	0.04	0.04
Na_2O	0.12	0.09	0.03	0.06	0.08	0.06	0.05	0.08	0.08	0.13	0.08
K_2O	8.89	8.69	9.12	7.82	7.64	8.12	7.17	8.93	9.26	9.00	8.71
H_2O*	4.10	4.07	3.66	3.66	3.66	3.76	3.78	—	3.77	3.75	3.75
Total	**99.21**	**98.35**	**95.70**	**95.22**	**95.55**	**98.17**	**98.78**	**93.74**	**99.45**	**99.04**	**96.49**
					Cations (22 O)						
Si	5.51	5.48	5.53	5.48	5.34	5.41	5.46	5.52	5.47	5.48	5.52
AlIV	2.49	2.52	2.47	2.52	2.66	2.59	2.54	2.48	2.53	2.52	2.48
ΣZ	8.00	8.00	8.00	8.00	8.00	8.00	8.00	8.00	8.00	8.00	8.00

Continued

AlVI	0.44	0.34	0.37	0.65	0.57	0.54	0.85	0.16	0.47	0.32	0.50
Ti	0.38	0.37	0.39	0.36	0.35	0.33	0.15	0.38	0.40	0.39	0.37
Fe^{2+}	3.31	3.18	3.45	3.59	3.61	3.59	3.80	3.05	3.72	3.73	3.91
Mg	1.35	1.61	1.48	1.12	1.32	1.34	0.98	2.00	1.07	1.26	0.85
Mn	0.03	0.02	0.02	0.02	0.02	0.03	0.08	0.05	0.04	0.04	0.07
ΣY	5.51	5.52	5.71	5.74	5.87	5.83	5.86	5.64	5.70	5.74	5.70
Ca	0.01	0.01	0.00	0.01	0.01	0.02	0.10	0.01	0.00	0.01	0.01
Na	0.04	0.03	0.01	0.02	0.03	0.02	0.02	0.02	0.02	0.04	0.02
K	1.76	1.73	1.91	1.63	1.59	1.65	1.46	1.82	1.88	1.84	1.84
ΣX	1.81	1.77	1.92	1.66	1.63	1.69	1.58	1.85	1.90	1.89	1.87
Parameters											
Fe/(Fe + Mg)	0.71	0.66	0.70	0.76	0.73	0.73	0.80	0.60	0.78	0.75	0.82
X_{Ann} (divalent)	0.71	0.66	0.70	0.76	0.73	0.73	0.80	0.60	0.78	0.75	0.82
T_{Henry} (˚C)	695	680	692	684	676	668	535	678	698 ± 6	702 ± 13	680 ± 3
T_{Luhr} (˚C)	705	698	702	683	680	674	540	708	631 ± 4	630 ± 8	620 ± 2
P_{Uchida} (kbar)	4.7	4.4	4.3	5.5	5.7	5.3	6.4	3.6	2.55 ± 0.14	2.07 ± 0.10	2.49 ± 0.10
Depth (km)	~17	~16	~16	~20	~21	~20	~24	~13	~9.4	~7.7	~9.2

Note. FeO* represents converted total iron. Formulae normalized to 22 positive oxygen equivalents.

- Single-point calculations across 12 analytical points for the Lakhar suite rock A-39N [23], and 12 points for the Kudri Hills suite demonstrate internal consistency:
- **Lakhar Suite (A-39N):** X_{Ann} = 81.8 - 83.6 mol% (mean 82.3 mol%), T_{Henry} = 672.4˚C - 684.5˚C (mean 680.3˚C ± 3.1˚C), T_{Luhr} = 614.2˚C - 622.1˚C (mean 619.6˚C ± 2.0˚C), and P_{Uchida} = 2.24 - 2.69 kbar (mean 2.49 ± 0.11 kbar or 2490 bars) (**Figure 8**).
- **Kudri Leucosome (Points 1 - 6):** X_{Ann} = 76.9 - 78.5 mol% (mean 77.7 mol%), T_{Henry} = 689.8˚C - 706.7˚C (mean 698.1˚C ± 5.7˚C), P_{Uchida} = 2.44 - 2.83 kbar (mean 2.55 ± 0.14 kbar) (**Figure 8**).
- **Kudri Melanosome (Points 7 - 12):** X_{Ann} = 73.8 - 74.9 mol% (mean 74.7 mol%), T_{Henry} = 678.9˚C - 717.3˚C (mean 702.1˚C ± 12.6˚C), P_{Uchida} = 1.92 - 2.20 kbar (mean 2.07 ± 0.10 kbar), (**Figure 8**).

The ternary plot of biotite show (**Figure 9**) that all the uriniferous pegmatoid Leucosomes and melanosomes are Fe-Mn rich annite to Siderophilite fields specially Lakhar and Anjangira Deohar (AD-24). These compositions are consistent with partial melting and melt-residue segregation under water-bearing crustal conditions, as constrained experimentally for granitic melts [37].

Thermobarometric reconciliation indicates two distinct crustal regimes (**Table 5**, **Figure 10**, and **Figure 11**):

1) Mid-Crustal Syn-Kinematic PLM (3.6 - 5.7 kbar, 668˚C - 695˚C): Recorded by Jaurahi, Jura, and Anjangira-Deohar, corresponding to emplacement depths of 13 - 21 km along ductile shears during *M*3 Grenvillian overprinting

(Figure 10). The estimated pressure-temperature conditions are compatible with the generation and migration of hydrous granitic melts in the middle crust [37].

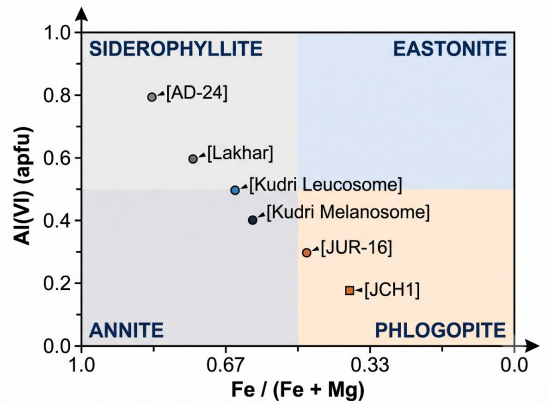


Figure 8. Fe/(Fe + Mg) Vs Al VI apfu plot for biotite composition in various pegmatoid leucosomes and melanosomes in Dudhi Group.

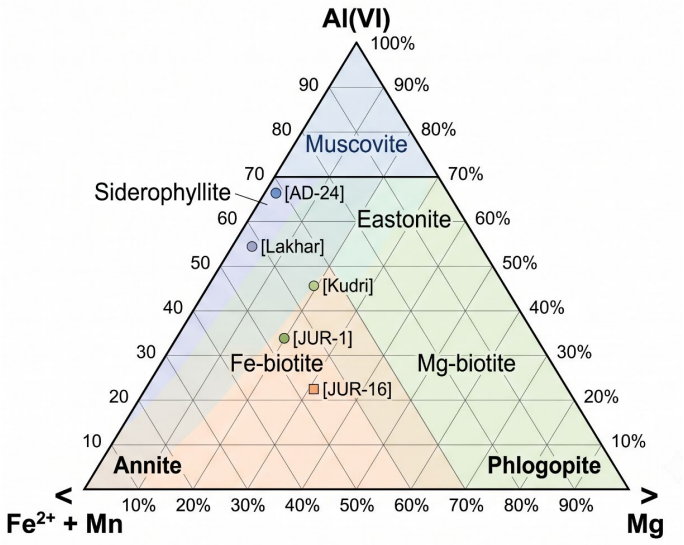


Figure 9. Ternary classification of Biotite of Dudhi group belonging to Fe-Mn rich Annite to Siderophyllite fields.

Table 5. Chemical and thermobarometric data for biotite from Dudhi group.

Suite / Sample	X_{Ann} (%)	X_{Phl} (%)	Ti/Fe^{2+}	T_{Luhr} (1984) (˚C)	T_{Henry} (2005) (˚C)	Altot (apfu)	P_{Uchida} (2007) (kbar)	Petrogenetic Interpretation
Lakhar (A-39N)	82.3%	17.7%	0.0945	619.6	680.3	2.98	2.49	High-grade S-type leucosome
Kudri Leucosome	77.8%	22.2%	0.1051	629.4	693.4	3.00	2.56	Upper-amphibolite anatexis
Kudri Melanosome	74.7%	25.3%	0.1048	629.1	697.8	2.85	2.11	Restitic melanosome selvedge
Jura JUR-1	70.0%	30.0%	0.1114	636.9	701.2	2.81	1.98	Uraniferous pegmatoid melt
Jura JUR-16	59.6%	40.4%	0.1250	649.2	722.5	2.75	1.80	Fractionated pegmatoid vein
Jaurahi JCH1	68.7%	31.3%	0.1163	640.7	707.1	2.70	1.65	Radioactive PLM facies
Anjangira AD-24	76.2%	23.8%	0.0784	603.3	664.5	3.17	3.07	Deeper crustal shear/pegmatite
Average (*Formula*)	**72.8%**	**27.2%**	**0.1051**	**629.7**	**695.3**	**2.89**	**2.24**	—

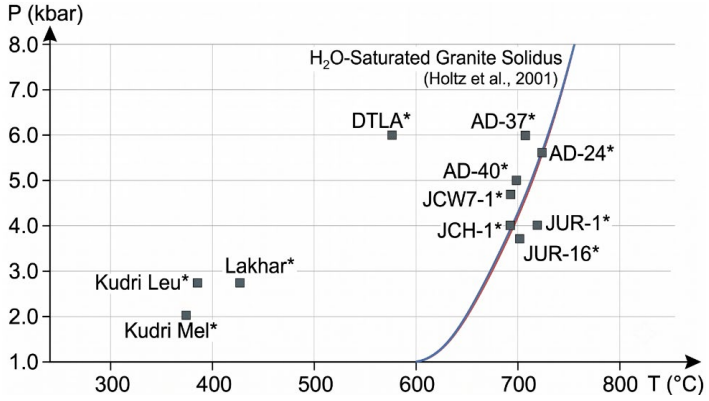


Figure 10. Pressure-temperature (*P-T*) crystallization diagram for the Dudhi Granitoid Complex biotites relative to the H_2O-saturated granitic solidus [37]. Primary pegmatoid leucosomes and host gneisses cluster between 590˚C and 708˚C at 2.5 - 5.7 kbar. Dolatola (DTLA) records lower-temperature subsolidus alteration (~535˚C).

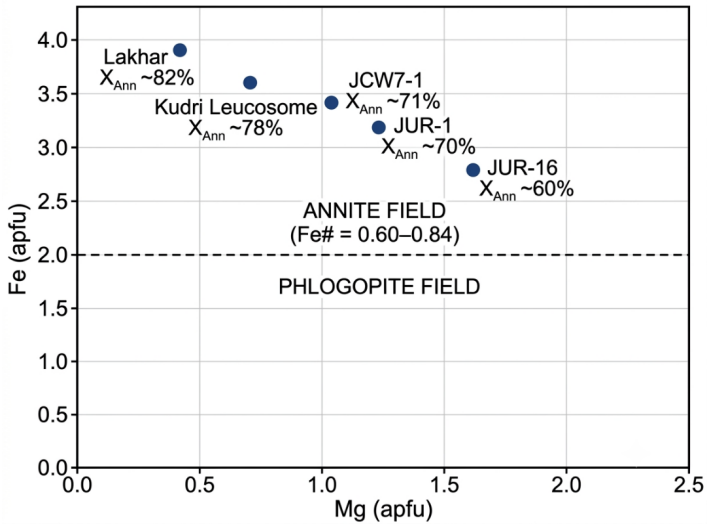


Figure 11. Octahedral Fe^{2+} vs. Mg classification diagram showing the clustering of Dudhi Granitoid Complex biotite within the annite field.

2) Upper-Crustal Pegmatoid Emplacement (2.07 - 2.55 kbar, 680˚C - 702˚C): Recorded by Kudri and Lakhar, reflecting shallower structural injection (~8 - 9.5 km depth) (Figure 10).

3) Subsolidus Retrograde Re-equilibration (535˚C - 540˚C, 6.4 kbar): Dolatola (DTLA-4-1) exhibits strongly suppressed TiO_2 (1.27 wt%) and elevated octahedral AlVI (0.85 apfu), recording *M*4 retrograde hydrothermal shear re-equilibration (Figure 10).

4.2. Feldspar Mineral Chemistry and Metasomatic Albitisation

Primary alkali feldspar is potassic, with orthoclase components spanning Or91.2-Or94.7 and barium contents of 0.16 - 0.26 wt% BaO (Table 6). Coexisting primary magmatic plagioclase corresponds to oligoclase-andesine (Ab65.5 - 67.2An32.3 - 33.9Or0.5 - 0.6). consistent with typical calc-alkaline to high-K granitoid compo-

sitions [38] [39].

Table 6. Electron microprobe compositions (wt%) and structural End-Members of feldspars (32-Oxygen Basis).

Parameter	JCH-1 Kfs (n = 9)	JCW7-1 Kfs (n = 7)	AD-24 Kfs (n = 5)	AD-37 Kfs (n = 5)	JCH-1 Magmatic Pl (n = 3)	JCH-1 Albitic Pl (n = 5)	JCW7-1 Magmatic Pl (n = 7)	JCW7-1 Albitic Pl (n = 2)
SiO_2	64.88 ± 0.45	65.59 ± 1.18	64.71 ± 0.52	64.83 ± 0.39	60.50 ± 1.25	67.45 ± 0.85	61.20 ± 1.10	68.10 ± 0.40
Al_2O_3	17.96 ± 0.18	18.40 ± 0.48	18.21 ± 0.09	18.41 ± 0.14	23.84 ± 0.45	20.04 ± 0.55	23.20 ± 0.60	19.50 ± 0.30
CaO	0.02 ± 0.01	0.01 ± 0.01	0.03 ± 0.02	0.06 ± 0.04	5.08 ± 0.85	0.41 ± 0.15	4.85 ± 0.95	0.18 ± 0.05
BaO	0.26 ± 0.08	0.18 ± 0.03	0.16 ± 0.05	0.18 ± 0.04	—	—	—	—
Na_2O	0.53 ± 0.13	1.38 ± 1.69	0.90 ± 0.41	0.89 ± 0.26	8.21 ± 0.45	10.86 ± 0.15	8.45 ± 0.50	11.10 ± 0.10
K_2O	14.83 ± 0.49	14.11 ± 2.42	14.56 ± 0.70	15.15 ± 0.39	0.10 ± 0.03	0.08 ± 0.03	0.14 ± 0.04	0.05 ± 0.02
Total	**98.48**	**99.67**	**98.57**	**99.52**	**97.73**	**98.84**	**97.84**	**98.93**
End-Members (mol%)								
Or	94.67 ± 1.25	94.50 ± 1.05	91.22 ± 3.38	91.28 ± 2.46	0.55 ± 0.15	0.45 ± 0.12	0.65 ± 0.20	0.28 ± 0.05
Ab	5.13 ± 1.20	5.45 ± 1.00	8.47 ± 3.45	8.17 ± 2.35	67.19 ± 8.20	96.05 ± 1.80	65.45 ± 7.50	97.40 ± 1.10
An	0.20 ± 0.15	0.05 ± 0.05	0.31 ± 0.19	0.55 ± 0.42	32.26 ± 8.10	3.50 ± 1.70	33.90 ± 7.40	2.32 ± 1.05

Note. Two metasomatised K-feldspar points in sample JCW7-1 (Or53.4Ab46.5 and Or67.3Ab32.6) track hydrothermal sodium metasomatism.

During *M*4 brittle reactivation along the SNSF corridor, pervasive hydrothermal sodic metasomatism (albitisation) overprinted the assemblage. Plagioclase was pseudomorphed by secondary albite (Ab96.1 - Ab97.4, An2.3 - An3.5), while K-feldspar in sheared mobilisate JCW7-1 was replaced along grain boundaries, driving orthoclase down to Or53.4. This coupled dissolution-reprecipitation reaction [40] [41]:

$$CaAl_2Si_2O_8\left(\text{in plagioclase}\right)+2Na^{+}+4SiO_2\left(aq\right)\rightarrow 2NaAlSi_3O_8\left(\text{albite}\right)+Ca^{2+}$$

released abundant Ca^{2+} into the hydrothermal fluid, directly sourcing the calcium required for Type-II uraninite metasomatism and alteration [42] [43].

The feldspar ternary relations, showing coexisting tie-lines between K-feldspar and primary magmatic plagioclase, as well as between K-feldspar and secondary albitic plagioclase (**Figure 12(a)**). The two-feldspar thermometric estimates in **Table 7** increase systematically with pressure from 1 to 5 kbar for all analysed pairs (**Figure 12(b)**) [44]. In samples JCH-1 and JCW7-1, pairs involving primary magmatic plagioclase yield higher temperatures than those involving secondary albitic plagioclase; for example, the calculated ranges are 367.9˚C- 404.8˚C and 322.0˚C-356.3˚C, respectively, in JCH-1, and 378.9˚C - 416.4˚C and 326.3˚C - 360.8˚C in JCW7-1. The estimates for AD-24 and AD-37, calculated using the mean magmatic-plagioclase composition as a reference, are higher still, ranging from 435.7˚C to 476.5˚C and 430.5˚C to 471.0˚C, respectively. These differences indicate that the secondary albitic assemblage records lower-temperature re-equilibration than the primary magmatic feldspar pairs, whereas AD-24 and AD-37 preserve com-

paratively higher apparent equilibration temperatures. The calculated values are interpreted as pressure-dependent estimates of feldspar re-equilibration or closure, rather than direct measurements of peak crystallisation temperature [45]-[47].

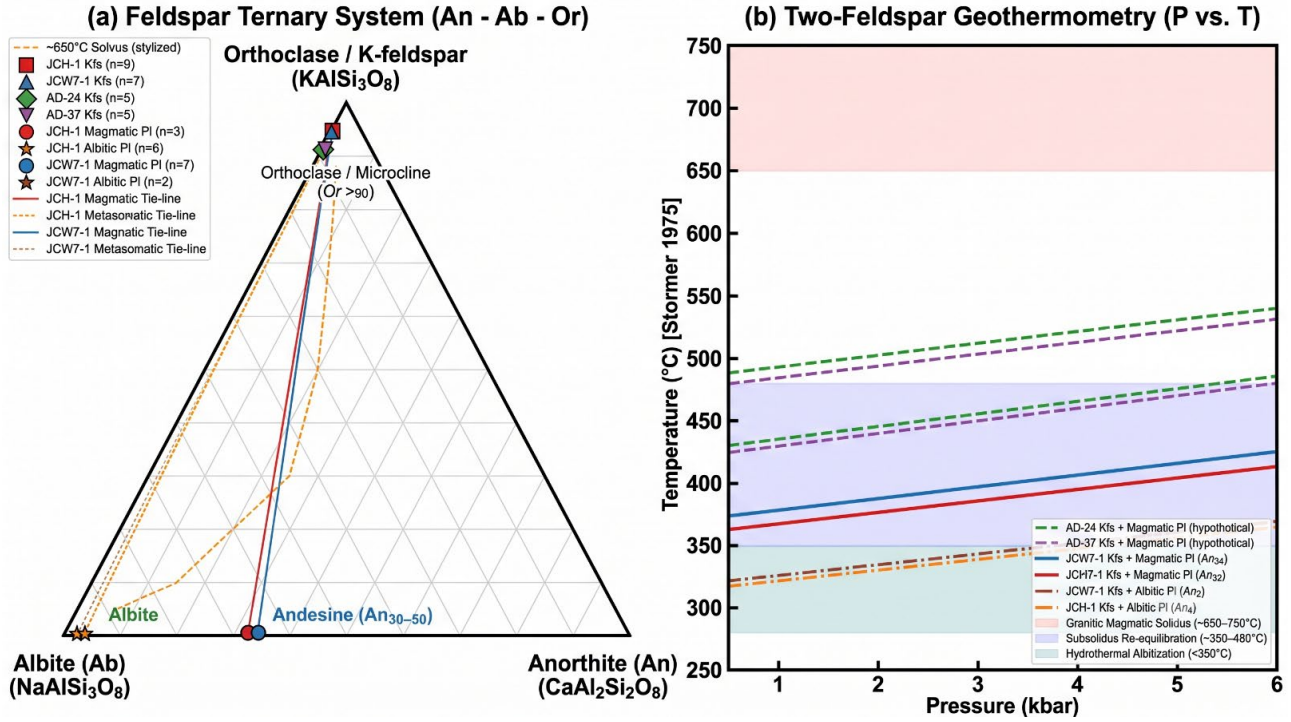


Figure 12. Feldspar Ternary System (Ab-An-Or): Showing coexisting tie-lines between K-feldspar and primary magmatic plagioclase, as well as between K-feldspar and secondary albitic plagioclase (a). (b) Two-Feldspar Geothermometry (*P* vs. *T*): Showing calculated closure and re-equilibration temperatures across crustal pressures (1 to 6 kbar) using the of Fuhrman, and Lindsley [44].

Table 7. Geothermobarometric calculation based on two feldspars.

Feldspar Pair	Composition (Ab)	*T* at 1 kbar (˚C)	*T* at 3 kbar (˚C)	*T* at 5 kbar (˚C)
JCH-1 (Kfs + Magmatic Pl)	$Ab_{Kfs} = 0.0513, Ab_{Pl} = 0.6719$	367.9	386.3	404.8
JCH-1 (Kfs + Albitic Pl)	$Ab_{Kfs} = 0.0513, Ab_{Pl} = 0.9605$	322.0	339.1	356.3
JCW7-1 (Kfs + Magmatic Pl)	$Ab_{Kfs} = 0.0545, Ab_{Pl} = 0.6545$	378.9	397.7	416.4
JCW7-1 (Kfs + Albitic Pl)	$Ab_{Kfs} = 0.0545, Ab_{Pl} = 0.9740$	326.3	343.6	360.8
AD-24 (Kfs + Magmatic Pl*)	$Ab_{Kfs} = 0.0847, Ab_{Pl} = 0.6632$	435.7	456.1	476.5
AD-37 (Kfs + Magmatic Pl*)	$Ab_{Kfs} = 0.0817, Ab_{Pl} = 0.6632$	430.5	450.7	471.0

*Note: AD-24 and AD-37 are evaluated against the mean magmatic plagioclase baseline (Ab0.6632) to evaluate relative thermal retention.

4.3. Petrological Interpretations

- **Subsolidus Thermal Re-equilibration:** Primary granitic magmas typically crystallize at solidus temperatures between 650˚C and 750˚C. Because the analyzed K-feldspars are depleted in the albite component (down to 5 - 8 mol%),

the calculated apparent temperatures of **~370˚C - 415˚C** indicate that high-temperature magmatic compositions were not preserved. Instead, the feldspars underwent prolonged subsolidus alkali exchange, exsolution, and continuous re-equilibration along the solvus during regional cooling [39] [46].

- **Hydrothermal Albitization:** The bimodal plagioclase distribution (andesine vs. albite) records a distinct two-stage thermal and fluid history:

1) An initial igneous stage responsible for the crystallization of primary andesine (An_{32-34}).

2) Infiltration of late- to post-magmatic, Na-rich aqueous fluids at temperatures below **~320˚C - 360˚C**, promoting metasomatic replacement and the precipitation of near-pure albite (An_{2-4}) [41].

- **Sample Suite Comparisons:** Samples **JCH-1** and **JCW7-1** re-equilibrated down to ~370˚C, reflecting complete subsolidus solvus purification. Conversely, samples **AD-24** and **AD-37** preserve elevated albite proportions in K-feldspar, yielding higher closure temperatures exceeding 430˚C. This indicates either earlier thermal closure during faster local cooling or less extensive interaction with post-magmatic metasomatic fluids [45] [46].

4.4. Zircon Trace-Element Systematics and CHIME Petrochronology

Accessory zircons demonstrate intense magmatic fractionation across the pegmatoid mobilisates (Table 8). Early magmatic zircons retain near-chondritic Zr/Hf ratios (33 - 36) and HfO_2 < 1.9 wt%, consistent with primitive to moderately evolved granitic melts [48] [49]. In fractionated leucosomes at Dolatola and late Jaurahi (JCW7-1), the Zr/Hf mass ratio collapses to 18.9 - 23.9, accompanied by extreme enrichment in HfO_2 (up to 2.75 wt%) and UO_2 (up to 1.98 wt% in AD-40). This marked decrease in the Zr/Hf ratio reflects advanced degrees of fractional crystallization in highly evolved, volatile-rich granitic systems [48] [50] [51].

Table 8. Representative microprobe compositions (wt%) and geochemical ratios of dudhi zircons (4-Oxygen Basis).

Oxide/Parameter	AD-40 (n = 9)	AD-37 (n = 10)	JCH-1 (n = 3)	JCW7-1 (n = 4)	Dolatola (n = 4)	Regional PLM (n = 14)
SiO_2	32.40 ± 0.65	31.85 ± 0.85	32.25 ± 0.40	32.10 ± 0.35	30.85 ± 0.70	31.35 ± 0.75
ZrO_2	62.40 ± 1.24	64.37 ± 1.63	63.30 ± 1.20	63.05 ± 1.04	61.50 ± 1.10	64.71 ± 1.46
HfO_2	1.59 ± 0.13	1.74 ± 0.14	1.85 ± 0.15	2.59 ± 0.32	2.75 ± 0.20	1.57 ± 0.18
UO_2	1.03 ± 0.72	0.49 ± 0.74	0.49 ± 0.22	0.43 ± 0.16	0.45 ± 0.15	0.68 ± 0.36
ThO_2	0.12 ± 0.07	0.14 ± 0.09	0.05 ± 0.04	0.04 ± 0.02	0.02 ± 0.01	0.11 ± 0.07
Y_2O_3	0.15 ± 0.15	0.07 ± 0.07	0.01 ± 0.01	0.07 ± 0.05	0.12 ± 0.04	0.12 ± 0.10
PbO*	1.30 ± 0.02	1.48 ± 0.02	0.00 ± 0.00	0.00 ± 0.00	0.00 ± 0.00	1.28 ± 0.02
Total	**96.89**	**99.35**	**100.96**	**98.01**	**96.81**	**99.02**
			Cations (4 O)			
Si^{4+}	0.663 ± 0.012	0.783 ± 0.035	0.667 ± 0.002	0.671 ± 0.008	0.655 ± 0.015	0.668 ± 0.010
Zr^{4+}	0.659 ± 0.007	0.453 ± 0.015	0.686 ± 0.002	0.660 ± 0.005	0.657 ± 0.008	0.672 ± 0.006

Continued

Hf^{4+}	0.010 ± 0.001	0.010 ± 0.001	0.011 ± 0.001	0.016 ± 0.002	0.017 ± 0.002	0.010 ± 0.001
U^{4+}	0.005 ± 0.003	0.004 ± 0.003	0.002 ± 0.001	0.002 ± 0.001	0.002 ± 0.001	0.003 ± 0.002
Th^{4+}	0.000	0.001 ± 0.001	0.000	0.000	0.000	0.000
			Tracers			
Zr/Hf (mass)	34.34 ± 3.12	32.26 ± 3.25	33.12 ± 2.85	21.29 ± 2.45	18.93 - 23.89	36.03 ± 4.25
Hf/(Hf + Zr)	0.015 ± 0.001	0.016 ± 0.002	0.015 ± 0.001	0.023 ± 0.002	0.025 ± 0.002	0.014 ± 0.002
Σ(U + Th + Y)	1.09 ± 0.75	0.71 ± 0.52	0.49 ± 0.20	0.43 ± 0.12	0.52 ± 0.15	0.69 ± 0.35

Note. PbO* represents total radiogenic lead measured by electron probe microanalysis (EPMA). Formulae normalized to 4 oxygens per formula unit.

Single-spot CHIME chemical dating [25] [35] of Lakhar zircon (Rock A-39N) confirms four discrete age populations (Table 9):

1) Inherited Xenocryst Cores: Point 7 (2892 ± 110 Ma) and Point 12 (2269 ± 85 Ma), recording Mesoarchaean and Palaeoproterozoic basement crust.

2) Palaeoproterozoic Anatectic Crystallization (*M*1): Point 11 (1846 ± 95 Ma), Point 3 (1835 ± 85 Ma), and Point 6 (1695 ± 95 Ma).

3) Mesoproterozoic Overprint: Point 8 (1402 ± 80 Ma) and Point 4 (1214 ± 70 Ma), corresponding to early Grenvillian thermal pulses.

4) Metamict Radiogenic Pb-Loss Zones: Points 1, 5, and 10 (116 - 159 Ma) and Point 9 (496 ± 75 Ma), caused by open-system lead loss where accumulated alpha radiation dose exceeded the critical amorphization threshold ($D_c \approx 2 \times 10^{18}$ α events/g) [52]-[55].

Table 9. Single-Spot zircon CHIME chemical ages and structural formulae for lakhar gneiss (Sample A-39N).

Point	UO_2 (wt%)	ThO_2 (wt%)	PbO (wt%)	Si (apfu)	Zr (apfu)	Ca (apfu)	U (apfu)	Apparent Age (Ma)	Interpretation
1	1.12	0.05	0.02	0.963	0.980	0.077	0.009	148 ± 65	Metamict domain; radiogenic lead loss
2	0.50	0.05	0.00	0.942	1.050	0.025	0.004	—	PbO below detection limit
3	0.48	0.01	0.11	0.949	1.053	0.005	0.003	1835 ± 85	Syn-collisional anatectic core (*M*1)
4	0.68	0.10	0.10	0.932	1.037	0.020	0.005	1214 ± 70	Mesoproterozoic thermal event (*M*3)
5	0.52	0.06	0.01	0.923	1.034	0.050	0.004	159 ± 90	Metamict domain; radiogenic lead loss
6	0.38	0.09	0.08	0.960	1.011	0.003	0.003	1695 ± 95	Late Palaeoproterozoic cooling (*M*2)
7	0.37	0.00	0.14	0.991	0.935	0.002	0.003	2892 ± 110	Inherited Mesoarchaean xenocryst core
8	0.29	0.06	0.05	0.957	1.018	0.000	0.002	1402 ± 80	Mesoproterozoic resetting / overgrowth
9	0.50	0.04	0.03	0.938	1.048	0.033	0.004	496 ± 75	Early Palaeozoic/Pan-African disturbance
10	0.72	0.06	0.01	0.942	1.039	0.013	0.005	116 ± 60	High-U domain; recent lead loss
11	0.21	0.15	0.05	0.948	1.053	0.002	0.001	1846 ± 95	Palaeoproterozoic anatectic crystallization
12	0.52	0.13	0.15	0.947	0.956	0.006	0.004	2269 ± 85	Inherited early Palaeoproterozoic relict

Note. Chemical ages calculated via the CHIME algorithm following Suzuki and Adachi [25]. Atoms per formula unit (apfu) calculated on a 4-oxygen basis.

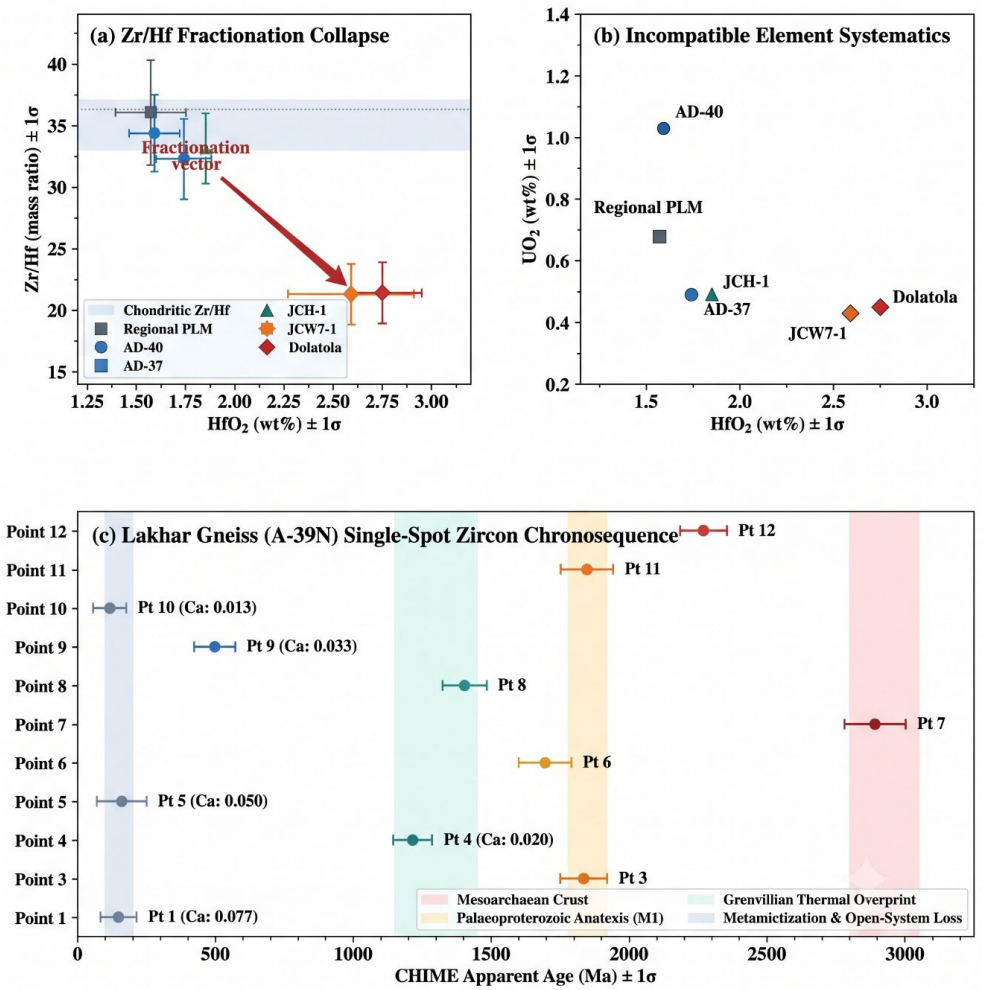


Figure 13. Geochemical systematics and microprobe CHIME petrochronology of accessory zircons from the Dudhi pegmatoid mobilisates and Lakhar gneiss (A-39N). **(a)** Mass Zr/Hf ratio vs. HfO_2 (wt%) demonstrating strong magmatic fractionation from near-chondritic early magmatic zircons (Zr/Hf~33 - 36) toward collapsed ratios in fractionated leucosomes (Dolatola, JCW7-1). **(b)** Incompatible element covariant plot of UO_2 vs. HfO_2 (wt%), isolating extreme U-enrichment in AD-40. **(c)** Single-spot zircon CHIME chemical age spectrum (Ma ± 1σ) identifying: (1) Mesoarchaean and Palaeoproterozoic basement inheritance, (2) syn-collisional anatectic crystallization (M_1, 1835--1846 Ma), (3) Mesoproterozoic thermal overprinting (~1.2 - 1.4 Ga), and (4) Phanerozoic lead loss in metamict domains marked by non-stoichiometric Ca ingress (Ca > 0.01 apfu).

Integrated zircon geochemical trends with single-spot CHIME ages to illustrate magmatic fractionation and the subsequent thermal and alteration history of the Dudhi pegmatoid mobilisates and Lakhar gneiss (A-39N). In panel (**Figure 13(a)**), the decline in Zr/Hf from the regional PLM and AD-40-AD-37 samples toward the Dolatola and JCW7-1 samples is consistent with progressive fractionation [48] [50] [51], while panel (**Figure 13(b)**) shows that AD-40 is distinguished by its comparatively high UO_2 content. The CHIME age distribution in panel (**Figure 13(c)**) records a complex chronology, including older basement inheritance, Palaeoproterozoic anatectic ages, a younger thermal overprint, and very young apparent ages associated with Ca-enriched, non-stoichiometric zircon spots. These

youngest values are interpreted as evidence of open-system disturbance and Pb loss in altered or metamict domains, rather than as reliable crystallization ages [54]-[57]. The combined data therefore suggest that the zircons preserve both the evolution of fractionated melts and a later, multistage history of crustal reworking and chemical disturbance. Zr/Hf variation is commonly used to assess magmatic fractionation, whereas Pb mobility in metamict zircon can compromise apparent age interpretations.

5. Results II: Uraninite Geochemistry, Crystallography, Metasomatism, and Chemical Dating

5.1. Primary Magmatic (Type-I) vs. Metasomatic (Type-II) Uraninite

Quantitative analyses of uraninites across the Dudhi Granitoid Complex delineate two fundamentally distinct populations (Table 10):

Table 10. Electron microprobe compositions (wt%) and chemical ages of uraninites across the dudhi belt.

Parameter	Kudri (n = 24)	Kudar (n = 27)	Naktu (n = 13)	Jhapar (n = 24)	Kurludih (n = 26)	Karke Chundi (n = 6)	Sirsoti (n = 9)	Lakhar (n = 9)	Anjangira I (n = 11)	Anjangira II (n = 6)
UO_2	76.83 - 84.13 (80.75)	75.69 - 80.97 (78.68)	75.87 - 80.36 (78.46)	74.72 - 79.60 (77.76)	76.01 - 81.57 (79.68)	73.66 - 78.93 (76.93)	81.69 - 85.56 (83.60)	73.42 - 83.93 (79.89)	81.36 - 83.21 (82.42)	71.44 - 78.40 (74.76)
ThO_2	2.25 - 6.35 (4.67)	4.70 - 6.91 (5.19)	5.39 - 7.03 (6.10)	5.39 - 7.75 (6.38)	4.93 - 5.74 (5.29)	5.47 - 7.27 (6.63)	3.70 - 5.55 (4.62)	3.48 - 7.00 (5.21)	3.10 - 4.79 (3.90)	2.65 - 4.19 (3.81)
PbO	9.31 - 11.52 (10.33)	9.50 - 11.45 (10.06)	9.58 - 11.01 (10.20)	9.06 - 11.05 (9.89)	9.58 - 10.76 (10.27)	8.35 - 9.17 (8.74)	9.87 - 10.53 (10.20)	8.18 - 10.86 (9.41)	9.30 - 10.16 (9.66)	7.02 - 9.44 (8.69)
CaO	0.06 - 0.62 (0.27)	0.32 - 1.25 (0.78)	0.32 - 0.84 (0.50)	0.21 - 1.00 (0.66)	0.38 - 1.59 (0.99)	0.60 - 0.86 (0.73)	0.24 - 0.95 (0.59)	0.14 - 1.15 (0.54)	0.16 - 0.46 (0.32)	3.66 - 10.69 (7.39)
SiO_2	<0.01 - 0.37 (0.07)	0.07 - 2.12 (0.57)	0.10 - 0.39 (0.21)	0.03 - 2.02 (0.39)	0.03 - 1.00 (0.28)	0.77 - 1.89 (1.27)	0.12 - 2.41 (0.59)	0.09 - 2.12 (0.62)	0.10 - 0.45 (0.22)	0.24 - 2.78 (0.99)
Y_2O_3	0.34 - 2.94 (1.37)	0.98 - 1.78 (1.44)	0.96 - 2.29 (1.59)	1.70 - 3.17 (2.31)	0.69 - 1.29 (0.94)	0.94 - 1.22 (1.07)	—	—	1.79 - 2.53 (2.05)	1.13 - 1.85 (1.44)
ΣRE_2O_3	0.96 - 2.43 (1.75)	1.36 - 2.37 (1.96)	1.48 - 2.94 (2.29)	1.80 - 2.70 (2.25)	1.69 - 2.52 (2.03)	1.35 - 2.18 (1.90)	—	—	1.38 - 2.10 (1.76)	0.93 - 2.10 (1.53)
Age Range (Ma)	**840 - 901**	**837 - 891**	**845 - 886**	**834 - 878**	**844 - 896**	**765 - 780**	**807 - 851**	**750 - 922**	**731 - 787**	**621 - 812**
Mean Age (Ma)	871	864	866	856	870	773	829	841 ± 62	751	731
Population Type	Type-I	Type-I	Type-I	Type-I	Type-I	Type-I	Type-I	Type-I	Type-I	Type-II
Habit/ Texture	Sub- to euhedral	Subhedral cubic	Euhedral cubic	Subhedral cubic	Subhedral cubic	Subhedral cubic	Subhedral cubic	Sub- to euhedral	Subhedral cubic	Corroded, chlorite rims

Note. Averages in parentheses. High-Ca uraninite data.

- **Type-I Primary Magmatic/Metamorphic Uraninite:** Preserved at Kudri, Kudar, Naktu, Jhapar, Kurludih, Sirsoti, Lakhar, and Anjangira Type-I. Characterized by high UO_2 (73.4 - 85.6 wt%), substantial ThO_2 (2.3 - 7.8 wt%), low CaO < 1.0 wt%, and low SiO_2 < 0.5 wt%. Chemical ages cluster tightly between

834 and 901 Ma across the Kudri sector, while Anjangira Type-I yields 731 - 787 Ma (mean 751 Ma).

- **Type-II Metasomatic High-Calcium Uraninite:** Identified at Anjangira [58]. Typified by extreme calcium enrichment (CaO = 3.66 - 10.69 wt%, mean 7.39 wt%), depressed UO_2 (71.44 - 78.40 wt%, mean 74.76 wt%), and lower PbO (7.02 - 9.44 wt%, mean 8.69 wt%). Chemical ages are discordantly younger, spanning 621 to 812 Ma (mean 731 Ma).

The elevated calcium content of Type-II uraninite demonstrates chemical exchange driven by hydrothermal fluids [59]-[61]. During M4 albitisation of plagioclase along the SNSF corridor, liberated Ca^{2+} cations substituted directly into the radiation-damaged fluorite lattice:

$$U^{4+} + 2O^{2-} \leftrightarrow Ca^{2+} + \square anions + O^{2-} \quad (8)$$

This lattice destabilization induced radiogenic lead loss, shifting apparent chemical ages from ~840 Ma toward 731 Ma.

5.2. Lakhar Uraninite Suite (Sample A-39)

Microprobe analyses of individual grains from Lakhar uraninite concentrate A-39 are partitioned into Low-Th and Medium-Th subgroups (**Table 11**, **Figure 14(a)**):

- **Low-Th Group (Points 1 - 4):** UO_2 = 80.96 - 83.93 wt% (mean 82.07 wt%), ThO_2 = 3.48 - 4.46 wt% (mean 3.87 wt%), PbO = 8.47 - 10.70 wt% (mean 9.81 wt%), CaO = 0.14 - 0.72 wt% (mean 0.43 wt%), and SiO_2 = 0.09 - 0.56 wt% (mean 0.24 wt%). Full decay ages span 750 - 906 Ma (mean 854 Ma [33] mean 819 Ma).
- **Medium-Th Group (Points 5 - 9):** UO_2 = 73.42 - 83.61 wt% (mean 78.14 wt%), ThO_2 = 5.24 - 7.00 wt% (mean 6.28 wt%), PbO = 8.18 - 10.86 wt% (mean 9.09 wt%), CaO = 0.34 - 1.15 wt% (mean 0.63 wt%), and SiO_2 = 0.18 - 2.12 wt% (mean 0.92 wt%). Full decay ages span 759 - 922 Ma (mean 830 Ma [33] mean 799 Ma).

Table 11. Microprobe analyses (wt%) and calculated U-Th-Pb chemical ages of Lakhar uraninites (Sample A-39).

Spot	Subgroup	UO_2	ThO_2	PbO	CaO	SiO_2	U	Th	Pb	Full Decay Age (Ma)	Cameron-Schiman Age (Ma)
1	Low Th	83.93	3.48	10.70	0.14	0.09	73.98	3.06	9.93	906	868
2	Low Th	82.22	3.91	10.07	0.38	0.12	72.48	3.44	9.35	875	839
3	Low Th	80.96	3.64	10.01	0.49	0.19	71.37	3.20	9.29	883	847
4	Low Th	81.16	4.46	8.47	0.72	0.56	71.54	3.92	7.86	750	722
5	Med Th	83.61	5.24	10.86	0.34	0.18	73.70	4.60	10.08	922	883
6	Med Th	80.17	5.97	8.67	0.51	0.42	70.67	5.25	8.05	778	747
7	Med Th	73.42	6.91	9.03	0.82	0.98	64.72	6.07	8.38	869	834
8	Med Th	75.88	7.00	8.74	0.34	0.89	66.89	6.15	8.11	823	792
9	Med Th	77.61	6.27	8.18	1.15	2.12	68.41	5.51	7.59	759	730
Mean	—	**79.89**	**5.21**	**9.41**	**0.54**	**0.62**	**70.42**	**4.58**	**8.74**	**841 ± 62**	**808 ± 57**

The sample mean age of 841 ± 62 Ma (1σ; [33] mean 808 ± 57 Ma) represents post-Grenvillian isotopic closure. The younger apparent ages in Point 4 (750 Ma) and Point 9 (759 Ma) directly correlate with elevated SiO2 (0.56 wt% and 2.12 wt%) and CaO (0.72 wt% and 1.15 wt%), reflecting minor radiogenic lead loss during hydrothermal alteration [58] [59].

Statistical comparisons between the Low-Th and Medium-Th subgroups:

- **Low-Th Group (n = 4, Spots 1 - 4):** UO_2 = 80.96 - 83.93 wt% (mean = 82.07 wt%); ThO_2 = 3.48 - 4.46 wt% (mean = 3.87 wt%); PbO = 8.47 - 10.70 wt% (mean = 9.81 wt%); CaO = 0.14 - 0.72 wt% (mean = 0.43 wt%); SiO_2 = 0.09 - 0.56 wt% (mean = 0.24 wt%). Full decay equation age spans 750 - 906 Ma (mean = 854 Ma).
- **Medium-Th Group (n = 5, Spots 5 - 9):** UO_2 = 73.42 - 83.61 wt% (mean = 78.14 wt%); ThO_2 = 5.24 - 7.00 wt% (mean = 6.28 wt%); PbO = 8.18 - 10.86 wt% (mean = 9.09 wt%); CaO = 0.34 - 1.15 wt% (mean = 0.63 wt%); SiO_2 = 0.18 - 2.12 wt% (mean = 0.92 wt%). Full decay equation age spans 759 - 922 Ma (mean = 830 Ma).

The Lakhar sample mean age of 841 ± 62 Ma (1σ) reflects Neoproterozoic crystallization and subsequent closure. The younger apparent ages in Spots 4 (750 Ma) and 9 (759 Ma) correlates with elevated SiO_2 (0.56 wt% and 2.12 wt%) and CaO (0.72 wt% and 1.15 wt%), indicating minor radiogenic lead loss caused by localized hydrothermal fluid-rock interaction.

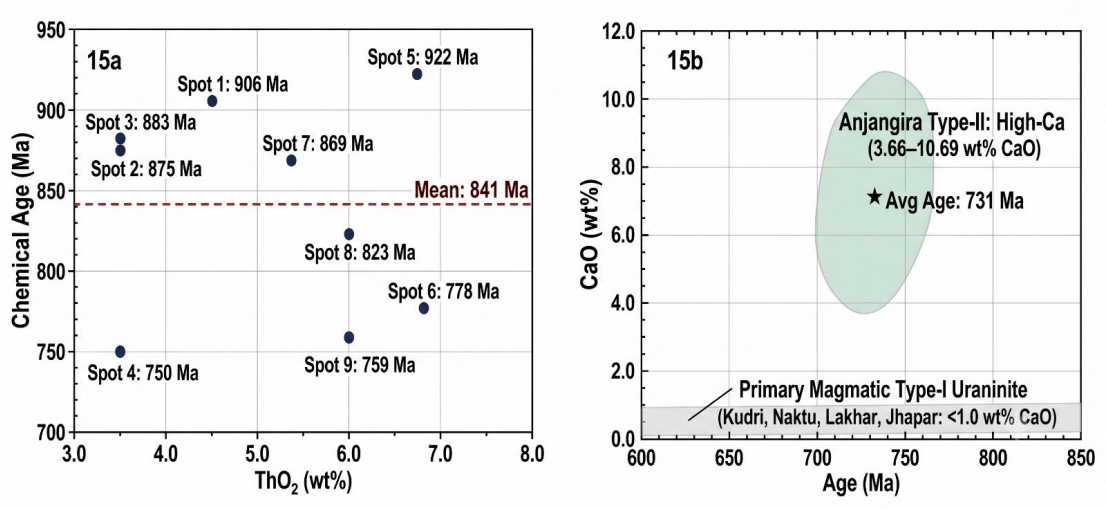


Figure 14. Uraninite chemical age (Ma) plotted against ThO_2 (wt%) for the Lakhar suite (Sample A-39). The mean age of 841 Ma is bracketed between 750 Ma and 922 Ma, with lower ages reflecting lead loss in altered domains (a). (b) Bivariate plot of CaO (wt%) vs. chemical age (Ma) showing the separation between primary magmatic uraninites (Type-I; 750 - 922 Ma) and metasomatic high-calcium uraninites (Type-II; 621 - 812 Ma).

The sample mean age of 841 ± 62 Ma (1σ) reflects Neoproterozoic crystallization and subsequent closure. The younger apparent ages in Spots 4 (750 Ma) and 9 (759 Ma) correlates with elevated SiO_2 (0.56 wt% and 2.12 wt%) and CaO (0.72 wt% and 1.15 wt%), indicating minor radiogenic lead loss caused by localized hy-

drothermal fluid-rock interaction. The CaO (wt%) against Age (Ma) to contrast two distinct uraninite populations (Figure 14(b)). The grey horizontal band at the base delineates primary magmatic Type-I uraninite, characterized by low calcium concentrations (<1.0 wt% CaO) across Kudri, Naktu, Lakhar, and Jhapar. In contrast, the prominent elliptical cluster highlights Anjangira Type-II uraninite, marked by significant calcium enrichment (3.66 - 10.69 wt% CaO) and an average chemical age centered at 731 Ma, reflecting a distinct secondary or hydrothermal alteration phase [42] [58].

5.3. Sirsoti Uraninite

Uraninite grains from the Sisroti occurrence (SIR_1 through SIR_9) demonstrates a remarkably uniform, pristine magmatic-pegmatoid composition (Table 12). The suite is characterized by elevated UO_2 concentrations ranging between 81.69 and 85.56 wt.% (mean 84.36 wt.%), robust ThO_2 contents of 3.70 to 5.55 wt.% (mean 4.54 wt.%), and radiogenic PbO accumulation between 9.87 and 10.53 wt.% (mean 10.25 wt.%). Low concentrations of alteration and metasomatic indicators—CaO (0.24 - 0.95 wt.%, mean 0.55 wt.%), SiO_2 (0.12 - 2.41 wt.%, mean 0.59 wt.%), TiO_2 (0.00 - 0.10 wt.%, mean 0.04 wt.%), and FeO (0.00 - 0.09 wt.%, mean 0.03 wt.%)—confirm the absence of intense sodic-calcic metasomatism or advanced supergene hydration.

Table 12. Spot mineral chemistry, cation partitioning, and chemical geochronology of Sisroti uraninite.

Spot No.	UO_2 (wt.%)	ThO_2 (wt.%)	PbO (wt.%)	CaO (wt.%)	SiO_2 (wt.%)	FeO (wt.%)	TiO_2 (wt.%)	U (apfu, 4O)	Th (apfu, 4O)	Pb (apfu, 4O)	tchem (Ma)	Paragenetic Status
SIR_1	85.56	5.15	10.25	0.39	0.13	0.02	0.03	1.782	0.110	0.258	818	Primary Leucosome Requisite
SIR_2	84.96	4.50	10.41	0.60	0.16	0.03	0.02	1.764	0.095	0.261	836	Primary Pegmatoid Domain
SIR_3	81.69	5.55	9.87	0.95	2.41	0.09	0.06	1.657	0.115	0.242	822	Incipient Silicate Infiltration
SIR_4	84.61	4.89	10.45	0.24	0.12	0.03	0.00	1.758	0.104	0.263	841	Pristine Leucosome Core
SIR_5	84.10	5.21	10.53	0.41	0.15	0.04	0.03	1.745	0.110	0.264	851	Pristine Leucosome Core
SIR_6	82.87	4.11	10.30	0.54	0.98	0.01	0.07	1.737	0.088	0.261	848	Primary Pegmatoid Domain
SIR_7	84.60	3.70	10.15	0.60	0.41	0.03	0.05	1.766	0.079	0.256	822	Primary Pegmatoid Domain
SIR_8	85.47	3.85	10.26	0.60	0.42	0.00	0.04	1.777	0.082	0.257	822	Primary Pegmatoid Domain
SIR_9	85.36	3.94	10.04	0.66	0.49	0.01	0.10	1.772	0.084	0.252	807	Primary Pegmatoid Domain
Average	**84.36**	**4.54**	**10.25**	**0.55**	**0.59**	**0.03**	**0.04**	**1.756**	**0.096**	**0.257**	**830**	**CGGC Neoproterozoic Suite**
Min	81.69	3.70	9.87	0.24	0.12	0.00	0.00	1.657	0.079	0.242	807	Lower Bound Envelope
Max	85.56	5.55	10.53	0.95	2.41	0.09	0.10	1.782	0.115	0.264	851	Upper Bound Envelope

*Note. Chemical ages (t_{chem}) calculated using the full iterative radiogenic lead accumulation equation of [26] and [34].

Structural Formula Normalization

1) Janeczek and Ewing's Method [29] Σcation = 1.000

Cations are normalized on the basis of one cation site ($\Sigma\text{cation} = 1.000$), with oxygen occupancy (ΣO) adjusting to maintain electroneutrality:

- **Sisroti (Average, $n = 9$):** $\left(U^{4+}_{0.814}Pb^{2+}_{0.119}Th^{4+}_{0.045}Ca^{2+}_{0.026}Si^{4+}_{0.026}Fe^{2+}_{0.001}Ti^{4+}_{0.001}\right)O_{1.85}$
- **Sisroti (SIR_1, Spot 1):** $\left(U^{4+}_{0.826}Pb^{2+}_{0.119}Th^{4+}_{0.051}Ca^{2+}_{0.018}Si^{4+}_{0.006}Fe^{2+}_{0.001}Ti^{4+}_{0.001}\right)O_{1.86}$
- **Sisroti (SIR_4, Spot 4—Lowest Ca-Si):** $\left(U^{4+}_{0.818}Pb^{2+}_{0.122}Th^{4+}_{0.048}Ca^{2+}_{0.011}Si^{4+}_{0.005}Fe^{2+}_{0.001}\right)O_{1.87}$
- **Sisroti (SIR_5, Spot 5—Peak Age):** $\left(U^{4+}_{0.811}Pb^{2+}_{0.123}Th^{4+}_{0.051}Ca^{2+}_{0.019}Si^{4+}_{0.007}Fe^{2+}_{0.001}Ti^{4+}_{0.001}\right)O_{1.86}$

2) Standard 4-Oxygen Stoichiometric Anion Basis (ΣO = 4.000)

Normalizing to 4 oxygens aligns Sisroti directly with the regional CGGC leucosome dataset:

- **Sisroti (Average, $n = 9$):** $\left(U_{1.756}Pb_{0.257}Th_{0.096}Ca_{0.055}Si_{0.055}Ti_{0.003}Fe_{0.002}\right)O_4$
- **Sisroti (SIR_1):** $\left(U_{1.782}Pb_{0.258}Th_{0.110}Ca_{0.039}Si_{0.012}Ti_{0.002}Fe_{0.002}\right)O_4$
- **Sisroti (SIR_3):** $\left(U_{1.657}Pb_{0.242}Th_{0.115}Si_{0.220}Ca_{0.093}Fe_{0.007}Ti_{0.004}\right)O_4$
- **Sisroti (SIR_4):** $\left(U_{1.758}Pb_{0.263}Th_{0.104}Ca_{0.024}Si_{0.011}Fe_{0.002}\right)O_4$

The petrogenetic discriminant diagrams in Figure 15 and Figure 16 together characterize the chemical maturity, genetic typology, and post-depositional alteration signatures of uraninite grains across the investigated occurrences. In Figure 16, the binary plots of UO_2 versus ThO_2 (A) and CaO versus SiO_2 (B) reveal that Sirsoti uraninites plot squarely within the pristine, unaltered primary magmatic field alongside Kudri and Anjangira-I, constrained by characteristically low calcium concentrations (CaO < 0.8 wt%), while sample SIR-3 shifts toward the silica axis due to minor intergranular silicate infiltration. Complementing these binary systematics, Figure 17 utilizes the ternary SiO_2-TiO_2-CaO discrimination space after Fritsche, and Dahlkamp [60] to classify the Didhi Group uraninites, effectively resolving primary high-temperature magmatic/pegmatitic affinities near the base from secondary hydrothermal or metasomatic overprints driven by calcium and titanium substitution, as well as silicate-bearing micro-inclusions.

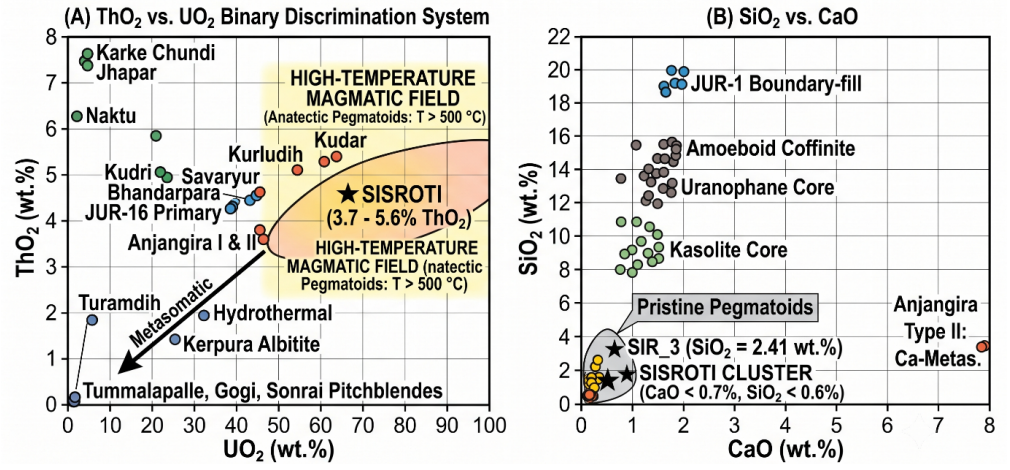


Figure 15. Petrogenetic discriminant diagrams UO_2 Vs ThO_2 (A), and CaO Vs SiO_2 (B). Sirsoti uraninites occupy the pristine unaltered field alongside Kudri and Anjangira-I (CaO < 0.8 wt%) whilst SIR-3 reflects minor intergranular silicate infilteration.

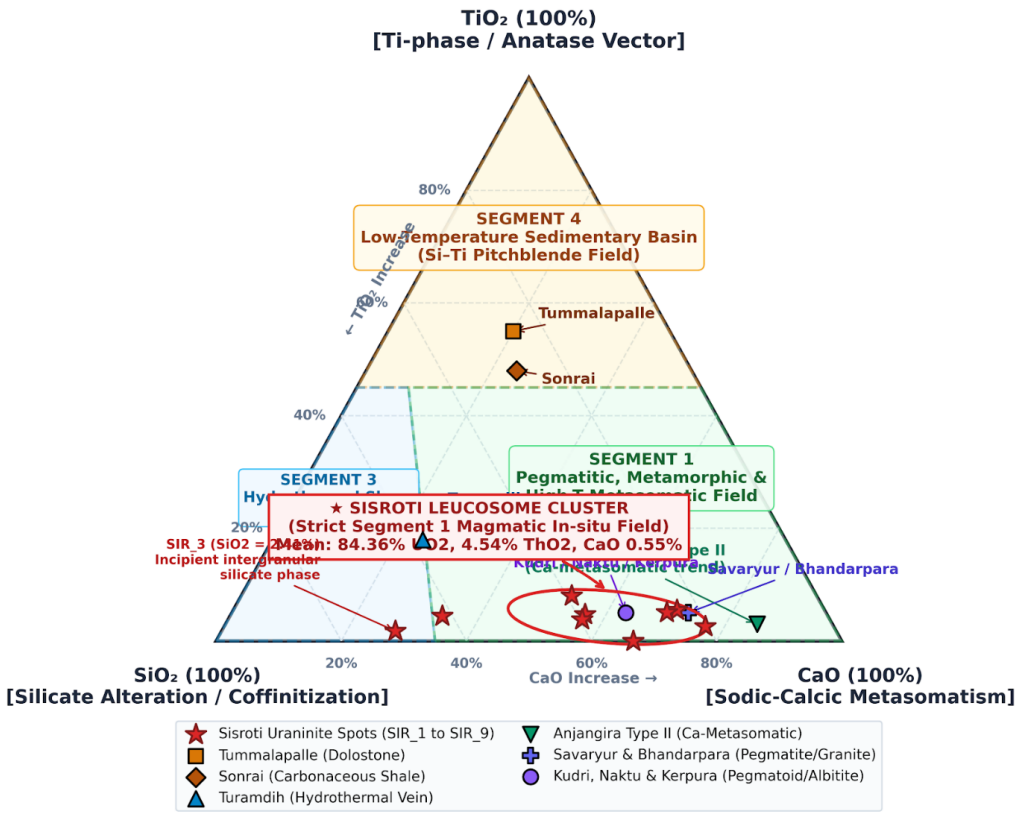


Figure 16. SiO_2-TiO_2-CaO Ternary diagram for uraninite of Dudhi Group. Petrogenetic discrimination after [60].

5.4. Formulation of U-Th-Pb Chemical Dating

Chemical dating of uraninite assumes that non-radiogenic common lead is negligible relative to the accumulated radiogenic lead (206Pb, 207Pb, 208Pb) generated by the decay of ^{238}U, ^{235}U, and ^{232}Th [26] [33] [34]. The full closed-system decay equation is expressed as:

$$\mathrm{Pb} = \mathrm{U}\left[\frac{0.9928}{238.03}\cdot 206\left(\mathrm{e}^{\lambda_{238}t}-1\right)+\frac{0.0072}{235.04}\cdot 207\left(\mathrm{e}^{\lambda_{235}t}-1\right)\right] + \mathrm{Th}\left[\frac{208}{232.04}\left(\mathrm{e}^{\lambda_{232}t}-1\right)\right] \tag{9}$$

Adopted decay constants [36] are:

$$\lambda_{238} = 1.55125\times 10^{-10}\ \mathrm{yr}^{-1} \tag{10}$$

$$\lambda_{235} = 9.8485\times 10^{-10}\ \mathrm{yr}^{-1} \tag{11}$$

$$\lambda_{232} = 4.9475\times 10^{-11}\ \mathrm{yr}^{-1} \tag{12}$$

Stoichiometric elemental conversion factors:

$$\mathrm{U} = \mathrm{UO_2}\times\frac{238.03}{270.03} \approx \mathrm{UO_2}\times 0.8815 \tag{13}$$

$$\mathrm{Th} = \mathrm{ThO_2}\times\frac{232.04}{264.04} \approx \mathrm{ThO_2}\times 0.8788 \tag{14}$$

$$\mathrm{Pb} = \mathrm{PbO} \times \frac{207.2}{223.2} \approx \mathrm{PbO} \times 0.9283 \tag{15}$$

The empirical approximation of [33] is given by:

$$t(\mathrm{Ma}) = (0.0884 \cdot \mathrm{U}) + (0.0245 \cdot \mathrm{Th})\mathrm{Pb} \times 10^3 \tag{16}$$

5.5. Comparative Petrochemical Systematics across Indian Uranium Terrains

Comparison with major Indian uranium provinces [58] highlights genetic differentiation (Table 13):

1) High-Temperature Magmatic/Pegmatitic Suites (>600˚C): Exemplified by Dudhi Type-I, Savaryur, and Bhandarpara. Typified by high ThO_2 (3 - 8 wt%), low SiO_2 < 0.5 wt%, and depleted CaO < 0.5 wt%.

2) Low-Temperature Hydrothermal/Basinal Suites (<200˚C): Exemplified by Tummalapalle (phosphatic dolostone), Gogi (epigenetic fault), and Sonrai (bituminous shale). Characterized by near-zero ThO_2 < 0.05 wt%, elevated SiO_2 (1.5 - 4.0 wt%), and high CaO (1.5 - 3.5 wt%).

3) Metasomatic Hybrid Suites: Typified by Anjangira Type-II, which retains high primary thorium (ThO_2 ≈ 3.8 wt%) inherited from the pegmatitic protolith while incorporating substantial calcium (CaO up to 10.69 wt%) via fluid-mediated coupled exchange as shown in equation 8.

Table 13. Compositional comparison of uraninites across Indian Proterozoic deposits [60].

Locality & Province	Lithological Host Formation & Facies	T (˚C)	UO_2 (wt%)	ThO_2 (wt%)	PbO (wt%)	CaO (wt%)	SiO_2 (wt%)	Chemical Age (Ma)	Coexisting Assemblage
Dudhi Type-I (Lakhar/Kudri)	Migmatite PLM	600 - 750	79.89	5.21	9.41	0.54	0.62	750 - 922	Zircon, annite, fluorapatite
Anjangira Type-II (Dudhi)	Sheared Metasomatic PLM	250 - 450	74.76	3.81	8.69	7.39	0.99	621 - 812	Albite, chlorite, calcite
Bhandarpara (CGGC)	Acid Plutonic Granite	700 - 850	72.29	5.22	9.64	0.29	0.45	~800 - 850	Monazite, xenotime, zircon
Savaryur (Dharwar Craton)	Granitic Pegmatite	650 - 750	83.59	4.69	6.65	0.43	0.17	~480 - 520	Uranothorite, pyrochlore
Turamdih (Singhbhum Shear Zone)	Hydrothermal Shear	400 - 550	74.06	1.18	16.36	0.13	0.57	>800	Chlorite, chalcopyrite, pyrite
Kerpura (Albitite Line, Rajasthan)	Sodic Metasomatite	400 - 500	84.66	1.00	9.95	0.37	0.19	~750 - 850	Albite, rutile, pyrite
Tummalapalle (Cuddapah Basin)	Carbonate Stratabound	100 - 180	82.74	0.02	4.78	2.84	3.71	157 - 402	Carbonate, pyrite, coffinite
Gogi (Bhima Basin)	Epigenetic Fault-Hosted	100 - 150	83.91	0.04	6.28	1.64	2.73	334 - 862	Bitumen, coffinite, galena
Sonrai (Bijawar Basin)	Bituminous Shale/Carb.	<120	88.60	0.00	5.07	1.80	1.54	51 - 607	Bitumen, chalcopyrite, pyrite

5.6. Uraninite Unit-Cell Refinements and Oxidation Systematics

Precision powder XRD refinements compiled across the Rihand Valley (Table 14) demonstrate that all primary uraninites occupy the metamorphic fluorite field (MTM), defined by cubic cell parameters $a_0 > 5.45$ Å [22].

Table 14. Unit-Cell dimensions, Unit-Cell volumes, and oxidation states of regional uraninites after [24].

Locality	Lithological Host	n	a_0 Range (A°)	Mean a_0 (A°)	Mean Volume V (A°³)	Formula Oxidation (FU)	Genetic Field
Rajon	Migmatite PLM	5	5.4653 - 5.4694	5.4675 ± 0.0015	163.44 ± 0.15	$UO_{2.006}$ - $UO_{2.04}$	MTM
Jaurahi	Migmatite PLM	1	—	5.4648	163.20	$UO_{2.05}$	MTM
Jura	Migmatite PLM	1	—	5.4638	163.11	$UO_{2.06}$	MTM
Naktu	Migmatite PLM	2	5.4566 - 5.4625	5.4596 ± 0.0030	162.73 ± 0.25	$UO_{2.07}$ - $UO_{2.12}$	MTM
Anjangira	Migmatite PLM	3	5.4542 - 5.4564	5.4561 ± 0.0010	162.33 ± 0.10	$UO_{2.13}$ - $UO_{2.15}$	MTM
Piparpan Nala	Granitoid	5	5.4485 - 5.4573	5.4529 ± 0.0035	162.14 ± 0.30	$UO_{2.11}$ - $UO_{2.19}$	MTM

The unit cell dimension exhibits a systematic inverse correlation with oxidation grade, contracting from pristine uraninite at Rajon (a_0 = 5.4675 Å, cell volume 163.44 Å^3, $UO_{2.02}$) to oxidised uraninite at Piparpan nala (a_0 = 5.4529 Å, cell volume 162.14 Å^3, $UO_{2.16}$). This fluorite lattice contraction results from the oxidation of larger U^{4+} (ionic radius ≈ 1.00 Å) to smaller U^{6+} (≈0.73 Å) and interstitial oxygen incorporation [31]. The preservation of $a_0 > 5.45$ Å confirms that these grains retain primary high-temperature crystalline structures that underwent post-crystallisation auto-oxidation without lattice breakdown [59] [61].

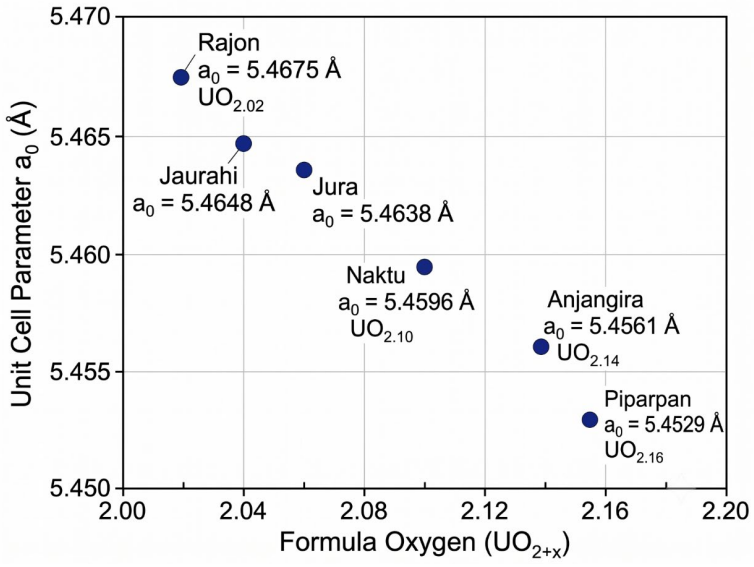


Figure 17. Empirical correlation showing the contraction of the uraninite fluorite lattice (a_0) as a function of the formula oxygen index (UO_{2+x}) across occurrences in the Rihand Valley.

The relationship between the unit cell parameter (a_0 in Å) and the degree of

oxidation expressed as formula oxygen (UO_{2+x}) for uraninite samples across different localities is displayed in Figure 17. A clear inverse linear correlation is displayed, where an increase in oxygen content—progressing from relatively pristine, near-stoichiometric uraninite at Rajon ($a_0 = 5.4675$ Å, $UO_{2.02}$) through Jaurahi ($a_0 = 5.4648$ Å), Jura ($a_0 = 5.4638$ Å), and Naktu ($a_0 = 5.4596$ Å, $UO_{2.10}$) to highly oxidized varieties at Anjangira ($a_0 = 5.4561$ Å, $UO_{2.14}$) and Piparpan ($a_0 = 5.4529$ Å, $UO_{2.16}$)—causes systematic lattice contraction. This unit cell shrinkage directly reflects the progressive oxidation of larger U^{4+} cations (ionic radius ~1.00 Å) to smaller U^{6+} cations (ionic radius ~0.73 Å), which induces structural distortion and lattice shrinkage during secondary alteration and auto-oxidation.

6. Discussion

6.1. Reconciling the Thermobarometric Datasets

Calculated biotite equilibration pressures exhibit a systematic bimodal distribution across the complex: the main PLM suite (Jaurahi, Jura, Anjangira-Deohar) records 4.3 - 5.7 kbar (~16 - 21 km), whereas Kudri and Lakhar record 2.07 - 2.55 kbar (~7.7 - 9.4 km).

This disparity reflects both analytical and geological controls:

1) Barometer Extrapolation Limits: The [34] calibration was derived from hornblende-bearing calc-alkaline suites. In iron-rich, low-Al metapelitic biotites, the barometer returns minimum bounding pressures.

2) Structural Emplacement Level: Melt extraction and injection were diachronous along the lithospheric SNSF shear zone. Kudri and Lakhar mobilisates represent higher-level, late-kinematic sheet intrusions emplaced into cooler, shallower crust (~8 - 10 km), whereas Anjangira-Deohar mobilisates equilibrated within deeper transpressional shear zones (~18 - 21 km).

The temperature record demonstrates remarkable regional coherence. Pegmatoid crystallization across seven localities clusters tightly between 668˚C and 702˚C. The anomalous 535˚C temperature at Dolatola represents subsolidus retrograde re-equilibration during *M*4 shear-zone reactivation.

6.2. Paragenetic Sequence and Secondary Uranyl Mineral Paragenesis

Textural relationships and mineral paragenesis document a three-stage sequence (Figure 18):

1) Primary Magmatic/Metamorphic Stage: Crystallization of stoichiometric uraninite (UO_2) and brannerite (UTi_2O_6) associated with sulfides (pyrite, chalcopyrite, molybdenite) and refractory high-field-strength oxides (davidite, fergusonite, columbite-tantalite).

2) Hydrothermal Metasomatic Stage (M4): Alteration along fractures and grain boundaries. Radiogenic lead released during fluid interaction combined with silica to form kasolite ($Pb(UO_2)SiO_4{\cdot}H_2O$). Alteration of biotite and ilmenite

contributed titanium to produce secondary brannerite, while sodic metasomatism supplied calcium to form Type-II high-Ca uraninite.

3) Supergene Alteration Stage: Uplift and exposure to oxygenated meteoric fluids converted primary oxides to uranyl silicate hydrates (uranophane, *β*-uranophane) in silica-saturated environments, and uranyl phosphates (autunite, meta-autunite, phosphuranylite) where accessory fluorapatite underwent acid-leaching.

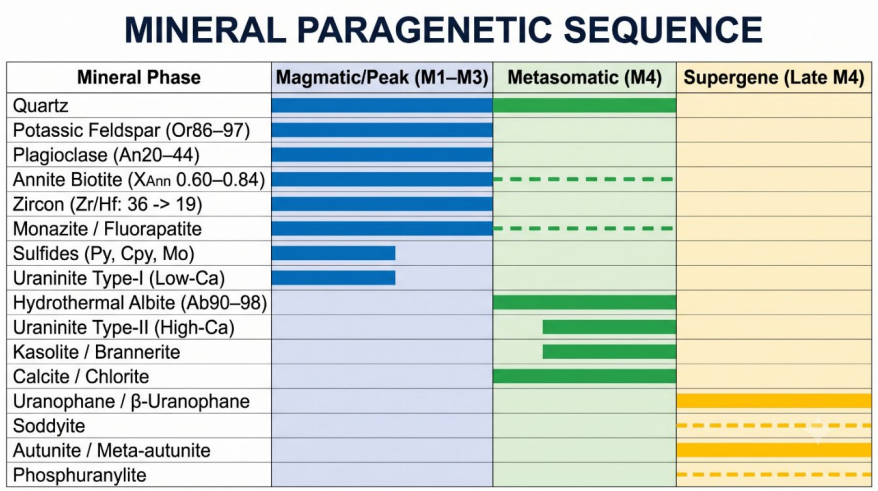


Figure 18. Paragenetic succession of primary rock-forming silicates, accessory minerals, and secondary alteration phases in the Dudhi Granitoid Complex.

6.3. Partitioning the Dual-Age Uranium Metallogeny

Integrating the EPMA chemical ages, zircon petrochronology, and field fabrics resolves the polyphase metallogenic evolution of the Dudhi Granitoid Complex (Figure 19):

- **Primary Anatexis and Melt Concentration (~1850 - 1630 Ma):** Collisional thickening along the CITZ drove partial melting of basement TTG and met-apelites at 750˚C - 940˚C and 5.5 - 7.5 kbar [38] [62]. Fluorine fluxing suppressed the solidus and prevented premature refractory oxide saturation [57] [63]. Incompatible uranium, thorium, and HFSE strongly partitioned into the extracted leucogranitic melt. Coexisting Kudri melanosome biotite acted as a restitic barrier, trapping refractory accessories (≤1200 ppm U, ≤656 ppm Th, and ≤3.1 wt% Zr). Primary zircon cores crystallised during this stage (1846 - 1835 Ma).
- **Grenvillian Annealing and Type-I Uraninite Closure (1200 - 950 Ma):** Transpressional shearing during the assembly of Rodinia re-equilibrated the silicates at 590˚C - 680˚C and 3.2 - 5.7 kbar under reducing conditions ($\log fO_2$ = −16.0 to −19.8 bars). Primary Type-I uraninites across Kudri, Kudar, Naktu, Jhapar, and Lakhar closed chemically during the waning stages of this event, preserving chemical ages of 834 - 901 Ma (Lakhar mean: 841 ± 62 Ma).
- **Brittle Reactivation and Metasomatism (950 - 600 Ma):** Brittle faulting along

the SNSF focused alkaline, sodic-calcic hydrothermal fluids at 250˚C - 450˚C (*D*5 - *M*4). Pervasive albitisation (Ab90 - 98) released calcium from magmatic plagioclase, driving calcium metasomatism of radiation-damaged uraninite to produce the Type-II population at Anjangira (mean age 731 Ma) and precipitating secondary kasolite.

- **Supergene Leaching (<600 Ma):** Uplift and meteoric fluid circulation induced auto-oxidation, fluorite lattice contraction ($UO_{2.01} \rightarrow UO_{2.19}$), and localized radiogenic lead loss in metamict zircon domains (116 - 159 Ma).

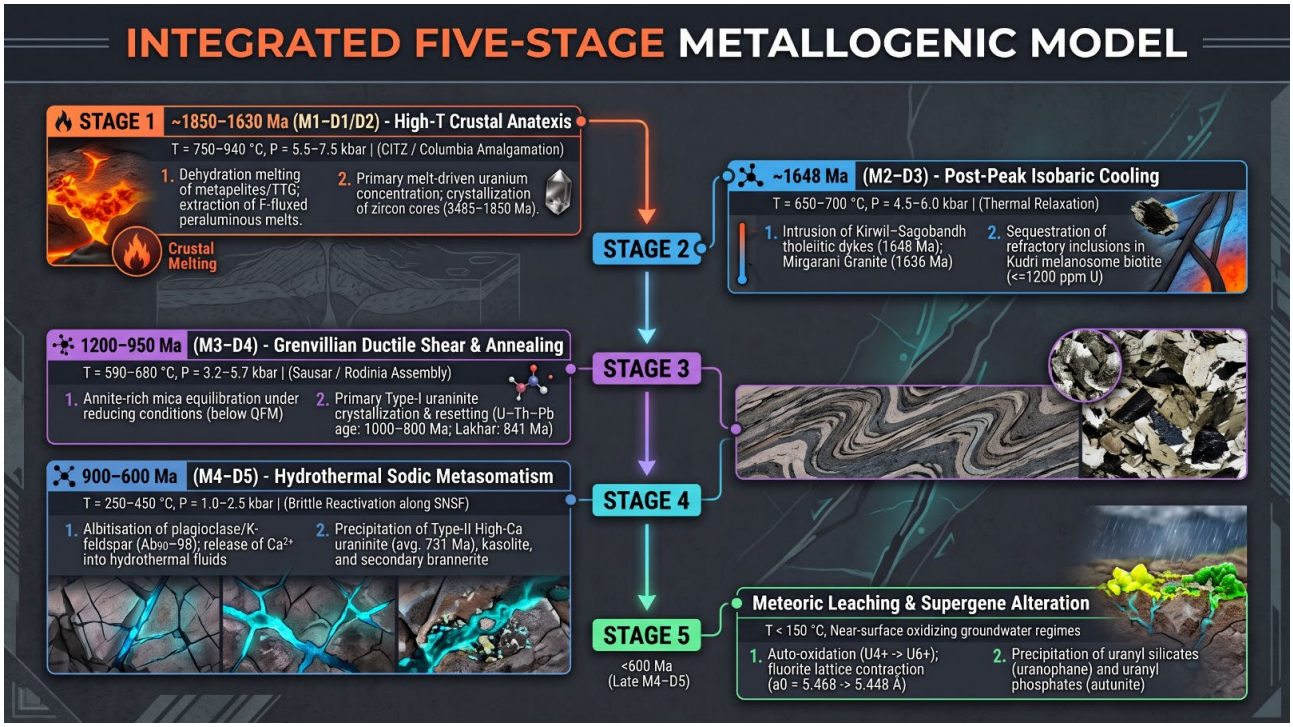


Figure 19. Schematic evolutionary model showing the five-stage metallogenic history of the Dudhi Granitoid Complex.

6.4. Exploration Vectors for the CGGC

The integrated findings provide a two-tier exploration model for uranium in the Chhotanagpur Granite Gneiss Complex:

1) Primary Magmatic Vector: Target highly fractionated PLM sheets characterized by biotite Fe/(Fe + Mg) > 0.75, zircon Zr/Hf < 25, elevated HfO_2 > 2.0 wt%, and pristine potassic feldspar (Or90 - 95).

2) Secondary Metasomatic Vector: Target the sheared, cataclastic margins of these sheets along the SNSF corridor, identified by intense albitisation (Ab > 95), calcium release, chloritization, Type-II high-Ca uraninite, and secondary kasolite.

7. Conclusions

1) The Dudhi Granitoid Complex records a protracted polymetamorphic (*M*1 - *M*4) and polydeformational (*D*1 - *D*5) history spanning from the Palaeoproterozoic assembly of Columbia to Phanerozoic fault reactivation.

2) Biotites across all leucosome mobilisates and melanosomes classify as annite-rich (X_{Ann} = 0.54 - 0.84; Fe/(Fe + Mg) = 0.60 - 0.82). Ti-in-biotite thermometry establishes primary crystallization at 668˚C - 695˚C (4.3 - 5.7 kbar) for the main PLM suite, 698˚C - 702˚C (2.07 - 2.55 kbar) at Kudri, and 680˚C (2.49 kbar) at Lakhar under reducing conditions ($\log fO_2$ = −16.0 to −19.8 bars). Retrograde re-equilibration is recorded at Dolatola (535˚C - 540˚C).

3) Metasomatic albitisation (Ab90 - 98) overprinted magmatic oligoclase-andesine (An20 - 44) and potassic feldspar (Or86 - 97), lowering orthoclase contents to Or53 and liberating Ca^{2+} into circulating hydrothermal fluids.

4) Zircons register pronounced fractionation, with Zr/Hf collapsing from 36 down to 18.9 at Dolatola, accompanied by HfO_2 enrichment up to 2.75 wt% and UO_2 up to 1.98 wt%. CHIME dating reveals inherited cores (2892 Ma, 2269 Ma), Palaeoproterozoic anatectic crystallization (1846 - 1835 Ma), and Mesoproterozoic resetting (1402 Ma, 1214 Ma).

5) Primary Type-I uraninite (UO_2 = 73.4 - 85.6 wt%, ThO_2 = 2.3 - 7.8 wt%, CaO < 1.0 wt%) records Grenvillian chemical ages of 834 - 901 Ma across the Kudri sector and Lakhar (841 ± 62 Ma). Hydrothermal fluid interaction along the SNSF precipitated metasomatic Type-II high-Ca uraninite at Anjangira (CaO = 3.66 - 10.69 wt%, chemical age 621 - 812 Ma, mean 731 Ma) and secondary kasolite.

6) Crystallographic XRD refinements confirm that regional uraninites occupy the metamorphic fluorite field (a_0 = 5.4485 - 5.4694 Å), undergoing systematic cell contraction in response to post-crystallisation auto-oxidation ($UO_{2.01} \rightarrow UO_{2.19}$).

Acknowledgements

This study synthesizes field investigations and analytical datasets generated under Project Son Valley, Atomic Minerals Directorate for Exploration and Research (AMD), Department of Atomic Energy (DAE), Government of India. The author expresses sincere gratitude to the EPMA and XRD laboratory teams for analytical support, and to colleagues for constructive scientific discussions.

Funding

This research received no external grant funding.

Conflicts of Interest

The author declares that there are no conflicts of interest.

References

[1] Bhattacharya, A.K., Gorikhan, R.A., Khazanchi, B.N., Fahmi, S., Singh, J. and Kaul, R. (1992) Uranium Mineralisation Hosted by Migmatite Mobilizate and Breccia Zones in the Northwestern Part of the Chotanagpur Granite Gneiss Complex, Rihand Valley, Sonbhadra District, Uttar Pradesh. *Indian Journal of Geology*, **64**, 259-275.

[2] Dhurandhar, A.P., Khirwal, S. and L.N. Sastry, D.V. (2023) Petrogenesis and Rb-Sr Isotopic Characteristics of Paleo-Mesoproterozoic Mirgarani Granite Sonbhadra Ut-

tar Pradesh India: Geodynamics Implication for Supercontinent Cycle. *Advances in Geological and Geotechnical Engineering Research*, **5**, 57-85. https://doi.org/10.30564/agger.v5i1.5261

[3] Acharyya, S.K. (2003) The Nature of Mesoproterozoic Central Indian Tectonic Zone with Exhumed and Reworked Older Granulites. *Gondwana Research*, **6**, 197-214. https://doi.org/10.1016/s1342-937x(05)70970-9

[4] Jain, S.C., Nair, K.K.K. and Yedekar, D.B. (1995) Geology of the Son-Narmada-Tapti Lineament Zone in Central India (Project Crumansonata) (Geological Survey of India Special Publication 10). Geological Survey of India, 8-10.

[5] Bhowmik, S.K., Wilde, S.A., Bhandari, A., Pal, T. and Pant, N.C. (2012) Growth of the Greater Indian Landmass and Its Assembly in Rodinia: Geochronological Evidence from the Central Indian Tectonic Zone. *Gondwana Research*, **22**, 54-72. https://doi.org/10.1016/j.gr.2011.09.008

[6] Mohanty, S. (2015) Precambrian Continent Assembly and Dispersal Events of South Indian and East Antarctic Shields. *International Geology Review*, **57**, 1992-2027. https://doi.org/10.1080/00206814.2015.1048751

[7] Chattopadhyay, A., Bhowmik, S.K. and Roy, A. (2020) Tectonothermal Evolution of the Central Indian Tectonic Zone and Its Implications for Proterozoic Supercontinent Assembly: The Current Status. *Episodes*, **43**, 132-144. https://doi.org/10.18814/epiiugs/2020/020008

[8] Černý, P., Meintzer, R.E. and Anderson, A.J. (1985) Extreme Fractionation in Rare-Element Granitic Pegmatites: Selected Examples of Data and Mechanisms. *The Canadian Mineralogist*, **23**, 381-421.

[9] Dahlkamp, F.J. (1993) Uranium Ore Deposits. Springer-Verlag.

[10] London, D. (2008) Pegmatites (Canadian Mineralogist Special Publication 10). Mineralogical Association of Canada.

[11] Pirajno, F. (1992) Hydrothermal Mineral Deposits: Principles and Fundamental Concepts for the Exploration Geologist. Springer-Verlag.

[12] Chhabra, J. and Kumar, D. (2002) Mineralogical and Chemical Features of Radioactive Biotites from Chhotanagpur Gneiss, Kudri Hills, Sonbhadra District, Uttar Pradesh. *Journal of the Geological Society of India*, **59**, 219-224. https://doi.org/10.17491/jgsi/2002/590304

[13] Mahendra Kumar, K., Bhattacharya, A.K., Gorikhan, R.A., Mathur, D.K. and Sen Gupta, B. (1998) Uranium Mineralisation Hosted by Albite-Rich Leucosome in the Migmatised Early Proterozoic Metasedimentary Rocks around Naktu, Son Valley, Sonbhadra District, U.P., India. *Exploration and Research for Atomic Minerals*, **11**, 55-60.

[14] Sengupta, B., Bhattacharya, A.K. and Subramanyam, A.V. (1998) Uranium Mineralisation in the Proterozoic Migmatites of Kudri-Lilasi, Sonbhadra District, U.P., India. *Journal of Atomic Mineral Science*, **6**, 127-133.

[15] Dhurandhar, A.P., Rajagopalan, V., Raminaidu, C., Parihar, P.S. and Gupta, R.K. (2003) Petrological and Geochemical Characterisation of Uraniferous Pegmatoid Leucosomes of Jura, District Sonbhadra, Uttar Pradesh, India. *Gondwana Geological Magazine*, **7**, 279-295.

[16] Dhurandhar, A.P., Rajagopalan, V. and Paul, A.K. (2025) Mineral Chemistry and Petrochronology of Zircon from Dudhi Group, Northwestern Chhotanagpur Granite Gneiss Complex, India. *Journal of the Geological Society of India*, **101**, 316-338. https://doi.org/10.17491/jgsi/2025/174098

[17] Dhurandhar, A.P., Latha, A. and Krishna, V. (2005) Geochronology and Petrochem-

istry of the Dubha Granite, Sonbhadra District, Uttar Pradesh. *Journal of the Geological Society of India*, **65**, 459-467. https://doi.org/10.17491/jgsi/2005/650407

[18] Dhurandhar, A.P., Srivastava, S.K., Sastry, D.V.L.N. and Parihar, P.S. (2006) Geochemistry and Geochronology of Metabasic Intrusions in the Kirwil-Sagobandh Area, Northwestern Chhotanagpur Terrane. *Indian Journal of Geology*, **78**, 119-134.

[19] Parihar, P.S. (2014) An Overview of Uranium, Rare Metal and REE Mineralization in the Crystallines of Sonbhadra District, Uttar Pradesh, India. IAEA Technical Document, URAM-2014, 179 p.

[20] Gupta, B.S., Paul, A.K. and Roy, M. (2005) A Rare Calcium Rich Uraninite from Anjangira Area, Sonbhadra District, Uttar Pradesh. *Journal of the Geological Society of India*, **65**, 296-300. https://doi.org/10.17491/jgsi/2005/650304

[21] Sinha, D.K., Sunil Kumar, T.S., Bandyopadhyay, S., Ranjan, R., Sarbjna, C., Lingamurty, E., Porwal, N., Sridhar, M. and Pandey, S. (2023) Leucosomal Zones in Chhotanagpur Granite Complex (CGGC), India: A Potential Host for Uranium and REE Mineralisation. *Exploration and Research for Atomic Minerals*, **30**, 1-16.

[22] Singh, Y. and Viswanathan, R. (2011) Atomic Mineral Occurrences and Mineralogical Crystallography of Uraninites in the Rihand Valley, Central India. *Exploration and Research for Atomic Minerals*, **21**, 41-63.

[23] Rajagopalan, V. and Paul, A.K. (2011) Role of Analytical Mineralogy of Major Primary Uranium and Thorium Minerals in Atomic Mineral Exploration in India. *Proceedings of International Conference* (*IAEA-DAE*) *on Peaceful Uses of Atomic Energy* 2009, New Delhi, 29 September-1 October 2009, 67-76.

[24] Kempe, U. (2003) Precise Electron Microprobe Age Determination in Altered Uraninite: Consequences on the Intrusion Age and the Metallogenic Significance of the Kirchberg Granite (Erzgebirge, Germany). *Contributions to Mineralogy and Petrology*, **145**, 107-118. https://doi.org/10.1007/s00410-002-0439-5

[25] Kato Suzuki, T. and Adachi, M. (1999) The Computer Program for the CHIME Age Calculation. *The Journal of Earth and Planetary Sciences*, *Nagoya University*, **46**, 49-56. http://www.nendai.nagoya-u.ac.jp/gsd/CHIME/

[26] Bowles, J.F.W. (1990) Age Dating of Individual Grains of Uraninite in Rocks from Electron Microprobe Analyses. *Chemical Geology*, **83**, 47-53. https://doi.org/10.1016/0009-2541(90)90139-x

[27] Deer, W.A., Howie, R.A. and Zussman, J. (2013) An Introduction to the Rock-Forming Minerals. 3rd Edition, Mineralogical Society of Great Britain and Ireland, 505 p.

[28] Tischendorf, G., Rieder, M., Förster, H.J., Gottesmann, B. and Guidotti, C.V. (2004) A New Graphical Presentation and Subdivision of Potassium Micas. *Mineralogical Magazine*, **68**, 649-667. https://doi.org/10.1180/0026461046840210

[29] Janeczek, J. and Ewing, R.C. (1992) Structural Formula of Uraninite. *Journal of Nuclear Materials*, **190**, 128-132. https://doi.org/10.1016/0022-3115(92)90082-v

[30] Henry, D.J., Guidotti, C.V. and Thomson, J.A. (2005) The Ti-SATURATION Surface for Low-to-Medium Pressure Metapelitic Biotites: Implications for Geothermometry and Ti-Substitution Mechanisms. *American Mineralogist*, **90**, 316-328. https://doi.org/10.2138/am.2005.1498

[31] Luhr, J.F., Carmichael, I.S.E. and Varekamp, J.C. (1984) The 1982 Eruptions of El Chichón Volcano, Chiapas, Mexico: Mineralogy and Petrology of the Anhydritebearing Pumices. *Journal of Volcanology and Geothermal Research*, **23**, 69-108. https://doi.org/10.1016/0377-0273(84)90057-x

[32] Uchida, E., Endo, S. and Makino, M. (2007) Relationship between Solidification

Depth of Granitic Rocks and Formation of Hydrothermal Ore Deposits. *Resource Geology*, **57**, 47-56. https://doi.org/10.1111/j.1751-3928.2006.00004.x

[33] Cameron-Schiman, M. (1978) Electron Microprobe Study of Uranium and Thorium Minerals from the Oklo Natural Fission Reactor and Other Occurrences. Ph.D. Thesis, University of Alberta.

[34] Montel, J., Foret, S., Veschambre, M., Nicollet, C. and Provost, A. (1996) Electron Microprobe Dating of Monazite. *Chemical Geology*, **131**, 37-53. https://doi.org/10.1016/0009-2541(96)00024-1

[35] Suzuki, K. and Adachi, M. (1991) Precambrian Provenance and Silurian Metamorphism of the Tsubonosawa Paragneiss in the South Kitakami Terrane, Northeast Japan, Revealed by the Chemical Th-U-total Pb Isochron Ages of Monazite, Zircon and Xenotime. *GEOCHEMICAL JOURNAL*, **25**, 357-376. https://doi.org/10.2343/geochemj.25.357

[36] Steiger, R.H. and Jäger, E. (1977) Subcommission on Geochronology: Convention on the Use of Decay Constants in Geo- and Cosmochronology. *Earth and Planetary Science Letters*, **36**, 359-362. https://doi.org/10.1016/0012-821x(77)90060-7

[37] Holtz, F., Johannes, W., Tamic, N. and Behrens, H. (2001) Maximum and Minimum Water Contents of Granitic Melts Generated in the Crust: A Reevaluation and Implications. *Lithos*, **56**, 1-14. https://doi.org/10.1016/S0024-4937(00)00056-6

[38] Dey, A., Karmakar, S., Ibanez-Mejia, M., Mukherjee, S., Sanyal, S. and Sengupta, P. (2020) Petrology and Geochronology of a Suite of Pelitic Granulites from Parts of the Chotanagpur Granite Gneiss Complex, Eastern India: Evidence for Stenian-Tonian Reworking of a Late Palaeoproterozoic Crust. *Geological Journal*, **55**, 2851-2880. https://doi.org/10.1002/gj.3552

[39] Nekvasil, H. (1994) Ternary Feldspar/Melt Equilibria: A Review. In: *Feldspars and their Reactions*, Springer Netherlands, 195-219. https://doi.org/10.1007/978-94-011-1106-5_5

[40] Putnis, A. (2002) Mineral Replacement Reactions: From Macroscopic Observations to Microscopic Mechanisms. *Mineralogical Magazine*, **66**, 689-708. https://doi.org/10.1180/0026461026650056

[41] Putnis, A. (2009) Mineral Replacement Reactions. *Reviews in Mineralogy and Geochemistry*, **70**, 87-124. https://doi.org/10.2138/rmg.2009.70.3

[42] Cuney, M. (2009) The Extreme Diversity of Uranium Deposits. *Mineralium Deposita*, **44**, 3-9. https://doi.org/10.1007/s00126-008-0223-1

[43] Polito, P.A., Kyser, T.K., Marlatt, J., Alexandre, P., Bajwah, Z. and Drever, G. (2004) Significance of Alteration Assemblages for the Origin Andevolution of the Proterozoic Nabarlek Unconformity-Related Uranium Deposit,northern Territory, Australia. *Economic Geology*, **99**, 113-139. https://doi.org/10.2113/gsecongeo.99.1.113

[44] Fuhrman, M.L. and Lindsley, D.H. (1988) Ternary-Feldspar Modeling and Thermometry. *American Mineralogist*, **73**, 201-215.

[45] Benisek, A., Kroll, H. and Cemič, L. (2004) New Developments in Two-Feldspar Thermometry. *American Mineralogist*, **89**, 1496-1504. https://doi.org/10.2138/am-2004-1018

[46] Parsons, I., Fitz Gerald, J.D., Lee, J.K.W., Ivanic, T. and Golla-Schindler, U. (2009) Time-Temperature Evolution of Microtextures and Contained Fluids in a Plutonic Alkali Feldspar during Heating. *Contributions to Mineralogy and Petrology*, **160**, 155-180. https://doi.org/10.1007/s00410-009-0471-9

[47] Yund, R.A. and Tullis, J. (1980) The Effect of Water, Pressure, and Strain on Al/Si

Order-Disorder Kinetics in Feldspar. *Contributions to Mineralogy and Petrology*, **72**, 297-302. https://doi.org/10.1007/bf00376148

[48] Bau, M. (1996) Controls on the Fractionation of Isovalent Trace Elements in Magmatic and Aqueous Systems: Evidence from Y/Ho, Zr/Hf, and Lanthanide Tetrad Effect. *Contributions to Mineralogy and Petrology*, **123**, 323-333. https://doi.org/10.1007/s004100050159

[49] Hoskin, P.W.O. and Schaltegger, U. (2003) The Composition of Zircon and Igneous and Metamorphic Petrogenesis. *Reviews in Mineralogy and Geochemistry*, **53**, 27-62. https://doi.org/10.2113/0530027

[50] Linnen, R.L. and Keppler, H. (2002) Melt Composition Control of Zr/Hf Fractionation in Magmatic Processes. *Geochimica et Cosmochimica Acta*, **66**, 3293-3301. https://doi.org/10.1016/s0016-7037(02)00924-9

[51] Wang, R.C., Xie, L., Chen, J., Yu, A., Wang, L., Lu, J.J. and Zhu, J.C. (2010) Extreme Fractionation of Granitic Melts: Evidences from Trace-Element and Y/Ho, Zr/Hf Ratios of Zircon. *Science China Earth Sciences*, **53**, 1845-1855.

[52] Ewing, R.C., Meldrum, A., Wang, L., Weber, W.J. and Corrales, L.R. (2003) Radiation Effects in Zircon. *Reviews in Mineralogy and Geochemistry*, **53**, 387-425. https://doi.org/10.2113/0530387

[53] Geisler, T., Pidgeon, R.T., Kurtz, R., van Bronswijk, W. and Schleicher, H. (2003) Experimental Hydrothermal Alteration of Partially Metamict Zircon. *American Mineralogist*, **88**, 1496-1513. https://doi.org/10.2138/am-2003-1013

[54] Geisler, T., Schaltegger, U. and Tomaschek, F. (2007) Re-Equilibration of Zircon in Aqueous Fluids and Melts. *Elements*, **3**, 43-50. https://doi.org/10.2113/gselements.3.1.43

[55] Nasdala, L., Wenzel, M., Vavra, G., Irmer, G., Wenzel, T. and Kober, B. (2001) Metamictisation of Natural Zircon: Accumulation versus Thermal Annealing of Radioactivity-Induced Damage. *Contributions to Mineralogy and Petrology*, **141**, 125-144. https://doi.org/10.1007/s004100000235

[56] Rayner, N., Stern, R.A. and Carr, S.D. (2004) Grain-Scale Variations in Trace Element Composition of Fluid-Altered Zircon, Acasta Gneiss Complex, Northwestern Canada. *Contributions to Mineralogy and Petrology*, **148**, 721-734. https://doi.org/10.1007/s00410-004-0633-8

[57] Keppler, H. (1993) Influence of Fluorine on the Enrichment of High Field Strength Trace Elements in Granitic Rocks. *Contributions to Mineralogy and Petrology*, **114**, 479-488. https://doi.org/10.1007/bf00321752

[58] Roy, M. and Roy, M. (2008) Temperature Dependent Textural and Chemical Variations in Uraninites from Diverse Geological Environments of India. *Journal of the Geological Society of India*, **72**, 155-167. https://doi.org/10.17491/jgsi/2008/720203

[59] Finch, R.J. and Ewing, R.C. (1992) Uraninite and UO_2 in Spent Nuclear Fuel: A Comparison. *Journal of Nuclear Materials*, **238**, 121-130. https://doi.org/10.1016/S0022-3115(96)00345-5

[60] Fritsche, R. and Dahlkamp, F.J. (1997) Contribution to the Characteristics of Uranium Oxides. Recent Developments in Uranium Resources and Supply (IAEA-TECDOC-961). International Atomic Energy Agency, 191-212.

[61] Frondel, C. (1958). *Systematic Mineralogy of Uranium and Thorium* (U.S. Geological Survey Bulletin 1064). U.S. Government Printing Office. https://doi.org/10.3133/b1064

[62] Spear, F.S. (1993) Metamorphic Phase Equilibria and Pressure-Temperature-Time

Paths. Mineralogical Society of America, 799 p.

[63] Aseri, A.A., Linnen, R.L., Che, X.D., Thibault, Y. and Holtz, F. (2015) Effects of Fluorine on the Solubilities of Nb, Ta, Zr and Hf Minerals in Highly Fluxed Water-Saturated Haplogranitic Melts. *Ore Geology Reviews*, **64**, 736-746. https://doi.org/10.1016/j.oregeorev.2014.02.014